

# The structure of massive star-forming galaxies from JWST and ALMA: Dusty, high-redshift disc galaxies

Steven Gillman<sup>1,2,\*</sup>, Ian Smail<sup>3</sup>, Bitten Gullberg<sup>1,2</sup>, A. M. Swinbank<sup>3</sup>, Aswin P. Vijayan<sup>1,2,4</sup>, Minju Lee<sup>1,2</sup>, Gabe Brammer<sup>1,5</sup>, Ugnė Dudzevičiūtė<sup>6</sup>, Thomas R. Greve<sup>1,2,7</sup>, Omar Almaini<sup>8</sup>, Malte Brinch<sup>1,2</sup>, Scott C. Chapman<sup>9</sup>, Chian-Chou Chen<sup>10</sup>, Soh Ikarashi<sup>11,12,13</sup>, Yuichi Matsuda<sup>11,14,15</sup>, Wei-Hao Wang<sup>10</sup>, Fabian Walter<sup>6,16</sup>, and Paul P. van der Werf<sup>17</sup>

<sup>1</sup> Cosmic Dawn Center (DAWN), Denmark

<sup>2</sup> DTU-Space, Elektrovej, Building 328, 2800 Kgs. Lyngby, Denmark

<sup>3</sup> Centre for Extragalactic Astronomy, Department of Physics, Durham University, South Road, Durham DH1 3LE, UK

<sup>4</sup> Astronomy Centre, University of Sussex, Falmer, Brighton BN1 9QH, UK

<sup>5</sup> Niels Bohr Institute, University of Copenhagen, Jagtvej 128, DK-2200 Copenhagen N, Denmark

<sup>6</sup> Max-Planck-Institut für Astronomie, Königstuhl 17, 69117 Heidelberg, Germany

<sup>7</sup> Dept. of Physics and Astronomy, University College London, Gower Street, London WC1E 6BT, United Kingdom

<sup>8</sup> School of Physics and Astronomy, University of Nottingham, Nottingham NG7 2RD, UK

<sup>9</sup> Dept of physics, Dalhousie University, Halifax, NS, Canada

<sup>10</sup> Academia Sinica Institute of Astronomy and Astrophysics (ASIAA), No. 1, Section 4, Roosevelt Road, Taipei 10617, Taiwan

<sup>11</sup> National Astronomical Observatory of Japan, 2-21-1 Osawa, Mitaka, Tokyo 181-8588, Japan

<sup>12</sup> Junior College, Fukuoka Institute of Technology, 3-30-1 Wajiro-higashi, Higashi-ku, Fukuoka 811-0295, Japan

<sup>13</sup> Department of Physics, General Studies, College of Engineering, Nihon University, 1 Nakagawara, Tokusada, Tamuramachi, Koriyama, Fukushima 963-8642, Japan

<sup>14</sup> Graduate University for Advanced Studies (SOKENDAI), Osawa 2-21-1, Mitaka, Tokyo 181-8588, Japan

<sup>15</sup> Cahill Center for Astronomy and Astrophysics, California Institute of Technology, MS 249-17, Pasadena, CA 91125, USA

<sup>16</sup> National Radio Astronomy Observatory, Pete V. Domenici Array Science Center, P.O. Box O, Socorro, NM 87801, USA

<sup>17</sup> Leiden Observatory, Leiden University, P.O. Box 9513, 2300 RA Leiden, The Netherlands

Received 5 June 2024 / Accepted 13 September 2024

## ABSTRACT

We present an analysis of the JWST NIRCam and MIRI morphological and structural properties of 80 massive ( $\log_{10}(M_*/[M_\odot]) = 11.2 \pm 0.1$ ) dusty star-forming galaxies at  $z = 2.7^{+1.2}_{-0.7}$ , identified as sub-millimetre galaxies (SMGs) by ALMA, which have been observed as part of the JWST PRIMER project. To compare the structure of these massive, active galaxies to more typical, less actively star-forming galaxies, we defined two comparison samples. The first of 850 field galaxies matched in specific star formation rate and redshift and the second of 80 field galaxies matched in stellar mass. From the visual classification of the SMGs, we have identified  $20 \pm 5\%$  as candidate late-stage major mergers, a further  $40 \pm 10\%$  as potential minor mergers, and  $40 \pm 10\%$  that have comparatively undisturbed disc-like morphologies, with no obvious massive neighbours on  $\lesssim 20\text{--}30$  kpc (projected) scales. These rates are comparable to those for the field samples and indicate that the majority of the sub-millimetre-detected galaxies are not late-stage major mergers, but have interaction rates similar to the general field population at  $z \sim 2\text{--}3$ . Through a multi-wavelength morphological analysis, using parametric and non-parametric techniques, we establish that SMGs have comparable near-infrared, mass-normalised sizes to the less active population,  $R_{50}^{\text{F444W}} = 2.7 \pm 0.2$  kpc versus  $R_{50}^{\text{F444W}} = 3.1 \pm 0.1$  kpc, but exhibit lower Sérsic indices, consistent with bulge-less discs:  $n_{\text{F444W}} = 1.1 \pm 0.1$ , compared to  $n_{\text{F444W}} = 1.9 \pm 0.1$  for the less active field galaxies and  $n_{\text{F444W}} = 2.8 \pm 0.2$  for the most massive field galaxies. The SMGs exhibit greater single-Sérsic fit residuals and their morphologies are more structured at  $2\,\mu\text{m}$  relative to  $4\,\mu\text{m}$  when compared to the field galaxies. This appears to be caused by significant structured dust content in the SMGs and we find evidence for dust reddening as the origin of the morphological differences by identifying a strong correlation between the F200W–F444W pixel colour and the  $870\,\mu\text{m}$  surface brightness using high-resolution ALMA observations. We conclude that SMGs and both massive and less massive star-forming galaxies at the same epochs share a common disc-like structure, but the weaker bulge components (and potentially lower black hole masses) of the SMGs result in their gas discs being less stable. Consequently, the combination of high gas masses and instabilities triggered either secularly or by minor external perturbations results in higher levels of activity (and dust content) in SMGs compared to typical star-forming galaxies.

**Key words.** galaxies: evolution – galaxies: high-redshift – galaxies: structure – submillimeter: galaxies

## 1. Introduction

The relative proportions of highly dust-obscured and less obscured star formation appears to vary over the history of

the Universe, with the dust-obscured component dominating in galaxy populations at  $z \sim 4\text{--}5$  down to the present day (e.g. Dunlop et al. 2017; Bouwens et al. 2020; Long et al. 2023). The cause of this transition in star formation mode may reflect the growing metallicity of the interstellar medium (ISM) in

\* Corresponding author; srigi@space.dtu.dk

galaxies, less efficient removal of dust from deeper potential wells, or structural or geometrical changes in the star-forming regions within galaxies.

The most extreme examples at high redshifts of systems dominated by dust-obscured star formation are the sub-millimetre galaxies (SMGs) with dust masses of  $M_d \sim 10^{8-9} M_\odot$  and far-infrared luminosities of  $L_{\text{IR}} \sim 10^{12-13} L_\odot$  (e.g. Magnelli et al. 2012; Rowlands et al. 2014; Miettinen et al. 2017b; Dudzevičiūtė et al. 2020), placing them in the ultra or hyperluminous infrared galaxy (U/HyLIRG) classes (see Hodge & da Cunha (2020) for a full review). Most of these galaxies show high star formation rates,  $\text{SFR} \sim 10^{2-3} M_\odot \text{ yr}^{-1}$  (e.g. Swinbank et al. 2014), and correspondingly short gas consumption timescales (e.g. Greve et al. 2005; Miettinen et al. 2017a; Tacconi et al. 2018; Birkin et al. 2021), suggesting that they represent relatively short-lived starbursts of  $\lesssim 100$  Myrs, which will result in massive systems with stellar masses of  $M_* \sim 10^{11} M_\odot$  (e.g. Wardlow et al. 2011; Simpson et al. 2014; Miettinen et al. 2017a; Dudzevičiūtė et al. 2020).

The high star formation rates and large stellar masses of SMGs have proved challenging to reproduce in theoretical galaxy formation models (e.g. Baugh et al. 2005; Swinbank et al. 2008; Hayward et al. 2013; McAlpine et al. 2019), although more recent attempts have been more successful (e.g. Lovell et al. 2022; Lower et al. 2023; Cochrane et al. 2024). The models suggest that the high star formation rates in this population are driven by a mix of secular instabilities in gas-rich discs and dynamical triggers due to minor and major mergers (e.g. McAlpine et al. 2019). However, attempts to observationally test these claims using the available rest-frame ultraviolet (UV) *Hubble* Space Telescope (HST) imaging of  $z \sim 1-3$  SMGs were challenging (e.g. Chapman et al. 2003). While the galaxies frequently exhibited irregular morphologies with apparently multiple components (e.g. Swinbank et al. 2010; Chen et al. 2015; Gómez-Guijarro et al. 2018; Zavala et al. 2018; Cowie et al. 2018; Lang et al. 2019; Ling & Yan 2022), their significant dust attenuation ( $A_V \gtrsim 2-6$ , e.g. Dudzevičiūtė et al. 2020) means that robustly assessing the intrinsic stellar mass morphology of the galaxies from these data was incredibly difficult. This is especially the case for the subset of the population that is undetectable in the near-infrared ('NIR-faint' SMGs, Simpson et al. 2014; Dudzevičiūtė et al. 2020; Smail et al. 2021; Ikarashi et al. 2022; Kokorev et al. 2023). Detecting and resolving the rest-frame near-infrared emission of SMGs, which is much less affected by dust attenuation and more closely traces the bulk of the stellar population, is essential to robustly constrain the morphology of their stellar mass. However, this has been beyond the reach of previous instrumentation such as the Infrared Array Camera (IRAC; Fazio et al. 2004) on the Spitzer Space Telescope, which, whilst providing the required near-infrared wavelength coverage from  $3.6-8 \mu\text{m}$ , lacked the sub-arcsecond spatial resolution required to constrain the underlying morphologies of the stellar emission in SMGs.

However, some progress has been made in understanding the structure of SMGs using high-resolution observations of the dust continuum and gas kinematics in SMGs (e.g. Simpson et al. 2015; Ikarashi et al. 2015; Fujimoto et al. 2017). Thus, full-width-at-half-maximum (FWHM)  $\sim 0'.1-0''.2$  sub-millimetre mapping with ALMA has revealed bright dust continuum emission arising from compact disc-like structures (i.e.  $R_e \sim 1-2$  kpc, Sérsic  $n \approx 1$ ) as well as evidence for a fainter, more extended component with  $R_e \approx 4$  kpc (e.g. Gullberg et al. 2019; Ivison et al. 2020). The bright compact component is roughly half the size of the galaxy extent in

HST *H*-band imaging (Hodge et al. 2016; Gullberg et al. 2019; Chen et al. 2020; Cochrane et al. 2021). At the highest resolutions, FWHM  $\sim 0''.05$ , Hodge et al. (2019) identified potential arms and bar-like structures in the bright dust continuum from a small sample of high-redshift SMGs.

Resolved kinematic studies using molecular and atomic fine structure emission lines in the rest-frame far-infrared and sub-millimetre have uncovered disc-like kinematics for at least a significant fraction of the population (e.g. Hodge et al. 2012; Chen et al. 2017; Lelli et al. 2021; Rizzo et al. 2021; Amvrosiadis et al. 2023). With the advent of the *James Webb* Space Telescope (JWST; Gardner et al. 2023), high-resolution observations from the near ( $1 \mu\text{m}$ ) to the mid-infrared ( $25 \mu\text{m}$ ) are now feasible, enabling the infrared emission from counterparts of sub-millimetre bright galaxies to be resolved and the issue of their stellar morphology and structures to be finally quantified.

Initial morphological studies with JWST have found size variations with wavelength in SMGs and less active colour-selected populations at  $z \sim 2$  (Chen et al. 2022; Cheng et al. 2023; Suess et al. 2022), with a reduction in the half-light radius when observed in the rest-frame near-infrared compared to the rest-frame UV/optical as previously studied with HST. A number of studies have subsequently expanded the samples with JWST and ALMA coverage, confirming that SMGs become more compact (higher concentration, smaller size) at longer wavelengths (e.g. Cheng et al. 2023; Gillman et al. 2023; Price et al. 2023) with the potential impact of dust on the observed morphology becoming less evident at longer wavelengths (e.g. Kokorev et al. 2022; Wu et al. 2023; Kamieneski et al. 2023; Sun et al. 2024). There are also claims of frequent stellar bars in many high-redshift star-forming galaxies (SFGs) (Guo et al. 2023; McKinney et al. 2024), including examples in SMGs (Smail et al. 2023). However, all of these studies suffer from modest sample statistics, limiting the interpretations of their findings.

In this paper, we present an analysis of the structural properties of a statistically robust sample of ALMA-detected, sub-millimetre-detected galaxies that have been observed with JWST NIRCam and MIRI. In Sect. 2, we define the sample of SMGs that we use in our analysis, whilst in Sect. 3 we present the observations, data reduction, and analysis undertaken on these systems (and matched control samples of less active galaxies selected from the field). In Sect. 4 we give our results and in Sect. 5 we discuss their implications, before summarising our main conclusions in Sect. 6. Throughout the paper, we assume a  $\Lambda$ CDM cosmology with  $\Omega_m = 0.3$ ,  $\Omega_\Lambda = 0.7$ , and  $H_0 = 70 \text{ km s}^{-1} \text{ Mpc}^{-1}$ . All quoted magnitudes are on the AB system and stellar masses are calculated assuming a Chabrier initial mass function (IMF) (Chabrier 2003).

## 2. Sample selection

To build a sample of ALMA-detected SMGs with near-infrared JWST coverage, we utilised the AS2UDS (Stach et al. 2019) and AS2COSMOS (Simpson et al. 2020) surveys as our parent sample. The AS2UDS and AS2COSMOS surveys are ALMA  $870 \mu\text{m}$  follow-up programmes of 716 and 180  $850 \mu\text{m}$  SCUBA-2 sources that are detected at  $>4\sigma$  in the S2CLS (Geach et al. 2017) map of the UKIDSS Ultra-Deep Survey (UDS; Lawrence et al. 2007) and the S2COSMOS (Simpson et al. 2019) map of the Cosmic Evolution Survey (COSMOS; Scoville et al. 2007), respectively. These two surveys provide an initial candidate sample of 896 SMGs with



**Fig. 1.** Combined AS2UDS and AS2COSMOS SMG sample in the PRIMER survey ranked in descending ALMA 870  $\mu\text{m}$  flux. For each SMG, we show the  $3'' \times 3''$  false colour image (F444W/F356W/F277W as R/G/B), labelled with the SMG ID, redshift (MAGPHYS derived,  $z_p$ , or spectroscopic,  $z_s$ ) and ALMA 870  $\mu\text{m}$  flux density. We further label the SMGs visually classified as major mergers (M) minor mergers or interactions (I), regular discs (D), or compact (C) as well as those potentially affected by gravitational lensing (Lens). The red cross indicates the ALMA 870  $\mu\text{m}$  position.

precise ALMA identifications, selected at  $S/N \geq 4$ , which we can use to characterise their near-infrared JWST counterparts.

We cross-matched the ALMA positions for the SMGs with the footprint of the JWST/NIRCam and JWST/MIRI observations from The Public Release IMaging for Extragalactic Research (PRIMER; Dunlop et al. 2021) survey. PRIMER is a multi-band, multi-instrument survey of UDS and COSMOS covering 234 and 144 sq. arcmin, respectively. The observations consist of the seven wide-band and one medium-band NIRCam filter (F090W, F115W, F150W, F200W, F277W, F356W, F410M, F444W) as well as two wide-band MIRI filters (F770W, F1800W). Parts of the UDS and COSMOS fields also benefit from HST ACS and WFC3 coverage from CAN-

DELS (Grogin et al. 2011) sampling the observed frame optical ( $0.4 \mu\text{m}$ ) to near-infrared ( $1.6 \mu\text{m}$ ).

For our analysis, we required the SMGs to be covered by the JWST/NIRCam long-wavelength (LW) filter F444W, ensuring that the observed-frame near-infrared was sampled. This results in a sample of 66 AS2UDS and 22 AS2COSMOS SMGs. A summary of the ALMA properties and HST and JWST coverage is presented in Appendix A. Of the 88 SMGs, 12 have no HST coverage. Two SMGs have JWST imaging in only three bands (F444W, F277W, and F200W), while the other 86 SMGs are covered by three or more JWST bands, with 37 SMGs having the maximum ten available JWST filters covering from 0.9 to 18  $\mu\text{m}$ , (Appendix A).

The 88 SMGs have a median ALMA 870  $\mu\text{m}$  flux of  $S_{870\mu\text{m}} = 3.8 \pm 0.4 \text{ mJy}$ , with a 16<sup>th</sup> to 84<sup>th</sup> percentile range of  $S_{870\mu\text{m}} = 1.8\text{--}6.1 \text{ mJy}$ , with the brightest, AS2COS0002.1, having  $S_{870\mu\text{m}} = 13.2 \text{ mJy}$  (see Appendix A). The SMGs sample the bulk of the AS2COSMOS and AS2UDS  $S_{870\mu\text{m}}$  distribution, which ranges from  $S_{870\mu\text{m}} = 0.6\text{--}19.2 \text{ mJy}$ . In addition, the majority of the AS2UDS SMGs (51/66) were observed with ALMA at resolutions of  $\simeq 0''.3$  FWHM, as is presented in Stach et al. (2019), with 15 SMGs observed at a higher resolution of  $\simeq 0''.2$  FWHM (see Gullberg et al. 2019). The ALMA maps of the 22 SMGs in the COSMOS field were tapered to a resolution of  $0''.8$  FWHM (Simpson et al. 2020).

### 3. Reduction and analysis

In this section, we present our data reduction and compilation of the photometric data that we used to characterise the multi-wavelength properties of the SMGs and their analysis.

#### 3.1. JWST and HST

We homogeneously processed the JWST NIRCam and MIRI observations, retrieving the Level-2 data products (version=jwst\_1069.pmap) from the STScI website<sup>1</sup> and processing them with the GRIZLI pipeline (Brammer & Matharu 2021; Brammer et al. 2022)<sup>2</sup>. For the NIRCam data, additional steps were employed to deal with diagonal striping seen in some exposures, cosmic rays, and stray light, whilst for the MIRI exposures time-dependent sky flats were applied in an approach similar to recent JWST studies (e.g. Yang et al. 2023). We further incorporated the available optical and near-infrared data available in the Complete *Hubble* Archive for Galaxy Evolution (CHARGE; Kokorev et al. 2022), providing multi-band imaging from 0.4 to 1.6  $\mu\text{m}$  for a subset of the sources (see Appendix A). We aligned all the imaging to Gaia DR3 (Gaia Collaboration & Brown 2021), co-added, and drizzled the final mosaics to a  $0''.04$  pixel scale (Fruchter & Hook 2002) for all JWST and HST filters.

#### 3.2. Photometry

For the JWST and HST bands, we extracted sources using SEP (Barbary et al. 2016), a PYTHON version of SOURCE EXTRACTOR (Bertin & Arnouts 1996), with a noise-weighted combined LW stacked (F277W+F356W+F444W) NIRCam image as the detection image. For each source, we made a cut-out in each of the HST and JWST bands, centred on this NIRCam LW detected source. Colour images made from the F444W/F356W/F277W NIRCam bands for the SMGs are shown in Fig. 1. Aperture photometry was performed in elliptical apertures with a minimum diameter of  $1''.0$  and corrected to the ‘total’ values following Kron (1980). The aperture corrections were computed on the NIRCam LW stacked image and applied to all bands. The MIRI observations were processed prior to the release of the updated photometric calibrations (August 2023). We thus scaled the measured flux in the F770W and F1800W bands by 0.85 and 1.03, respectively, following the JWST documentation. We determined a median F444W AB magnitude for the SMG sample of  $m_{\text{F444W}} = 21.7 \pm 0.3$  with a 16<sup>th</sup>–84<sup>th</sup> percentile range of  $m_{\text{F444W}} = 20.3\text{--}23.1$ .

We compiled the mid-infrared to radio (5.8  $\mu\text{m}$  to 1.4GHz) photometry for our sources from Dudzevičiūtė et al. (2020) and Simpson et al. (2020). For the SMGs with no MIRI F770W and F1800W imaging, we adopted the IRAC channel 3 (5.8  $\mu\text{m}$ ) and channel 4 (8  $\mu\text{m}$ ) photometry, if the IRAC channel 1 (3.6  $\mu\text{m}$ ) flux is within 10 percent of the NIRCam F356W and the IRAC channel 2 (4.5  $\mu\text{m}$ ) flux is within 10 percent of the NIRCam F444W. We employed the IRAC photometry for two out of seven AS2COSMOS SMGs without MIRI coverage and 11 out of 38 AS2UDS SMGs.

#### 3.3. Final sample

Having collated a sample of 88 AS2UDS and AS2COSMOS SMGs lying within the JWST PRIMER fields, we visually inspected each of the galaxies’ JWST imaging to verify the association of the near-infrared counterpart with the ALMA source. We removed three UDS sources (AS2UDS0106.0, AS2UDS0175.0, and AS2UDS0069.0) and three COSMOS sources (AS2COS0017.1, AS2COS0032.1, and AS2COS0035.1) due to partial coverage in the JWST NIRCam imaging. Of the remaining 82 SMGs, we identify one SMG, AS2UDS0490.0, with no clear NIRCam counterpart, with a F444W magnitude of  $m_{\text{F444W}} = 26.7 \pm 0.6$  detected at  $1.4\sigma$ . There is no MIRI coverage or any detection of this  $S_{870} = 2.7 \text{ mJy}$  ( $S/\text{N} = 4.5$ ) source between UV and radio, and thus we concluded that it is likely spurious, with the ALMA catalogue of 707 sources from Stach et al. (2019) expected to have a two percent spurious fraction, and so excluded the source from our sample. We also removed two SMGs, AS2COS0005.1 and AS2COS0005.2, which appear to be strongly gravitational lensed, and thus the derivation of their intrinsic properties including morphology would require detailed and uncertain lens modelling (e.g. Amvrosiadis et al. 2018; Bendo et al. 2023; Pearson et al. 2024). We also flagged AS2UDS0281.0 and AS2UDS0382.0 as possibly weakly lensed, opting to keep them in the sample.

Finally, one ALMA source from Simpson et al. (2020), AS2UDS00071.0, was deblended in the NIRCam F444W imaging, and high-resolution ALMA observations (Gullberg et al. 2019), into two sources that we have labelled AS2UDS00071.0a and AS2UDS00071.0b. We modelled the morphology of AS2UDS0071.0a and AS2UDS0071.0b independently and scaled the blended photometry by the flux ratio of the two sources. Thus, in the final sample, we have 80 SMGs, for each of which the HST and JWST coverage is detailed in Appendix A.

#### 3.4. Spectral energy distribution fitting

Having defined a final sample of 80 SMGs with robust near-infrared counterparts, we used the SED fitting code Multi-wavelength Analysis of Galaxy Physical Properties and Photometric Redshift (MAGPHYS+PHOTO-z, hereafter referred to as MAGPHYS; Cunha et al. 2015; Battisti et al. 2019) to derive the physical properties of each SMG<sup>3</sup>. For 22 of the SMGs spectroscopic redshifts are available from the literature and ongoing millimetre and near-infrared spectroscopic surveys (e.g. McLure et al. 2018; Mitsuhashi et al. 2021). For these sources, we used the high-redshift version of MAGPHYS,

<sup>1</sup> <https://mast.stsci.edu/>

<sup>2</sup> For full details of the reduction process see: <https://dawn-cph.github.io/dja/imaging/v7/>

<sup>3</sup> We note that we do not include an AGN component in the MAGPHYS modelling as the fraction with significant AGN contributions is expected to be small (e.g. Stach et al. 2019) (see Sect. 4).

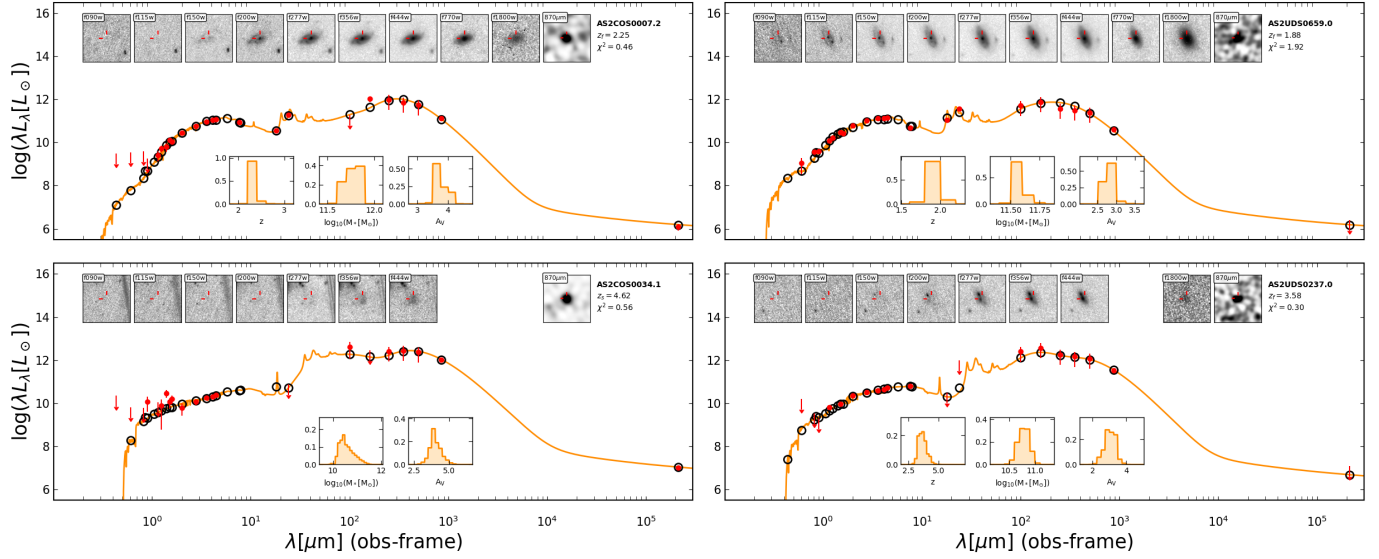


**Fig. 2.** Multi-wavelength SEDs for four example SMGs that demonstrate the range of observed-frame infrared colours displayed by the SMG sample. Appendix B shows the SEDs for the full sample. For each source, we indicate the observed flux and error in each band with a red circle and error bar. Arrows show upper limits at  $3\sigma$ . We over-plot the best-fit magphys derived SED (orange line) and model fluxes (black circles). Below each SED we display the probability distributions of the MAGPHYS derived properties: redshift (unless spectroscopic), stellar mass and  $A_V$ , and report the best-fit redshift and reduced  $\chi^2$  from the fit in the top right. Above the SED we display the multi-wavelength JWST and ALMA 870  $\mu\text{m}$  imaging used as part of the analysis, with the SMG centroid indicated by the red tick markers.

(MAGPHYS+HIGHz (v2); Cunha et al. 2015; Battisti et al. 2019) with the redshift fixed to the spectroscopic redshift of each source, as is detailed in Appendix A.

MAGPHYS is a physically motivated SED fitting code that utilises the energy balance technique to fit the multi-wavelength photometry from UV to radio. This approach, tested on SMGs by Cunha et al. (2015) and Dudzevičiūtė et al. (2020) and also on simulated galaxies (e.g. Dudzevičiūtė et al. 2020; Haskell et al. 2023), models the sub-millimetre and optical emission as originating from the same region of the galaxy (for a discussion of using the magphys SED code to model high-redshift SMGs, we refer the reader to Dudzevičiūtė et al. 2020). For consistencies with Dudzevičiūtė et al. (2020), for non-detections at wavelengths shorter than 8  $\mu\text{m}$ , we adopted a  $3\sigma$  upper limit, while for those beyond 10  $\mu\text{m}$ , we used  $1.5 \pm 1.0\sigma$ .

In Fig. 2, we show examples of the multi-wavelength photometry and magphys SED fits, with the fits for the whole sample presented in Appendix B. We summarise some of the key derived physical properties of the SMG sample in Fig. 3. We estimate a median redshift of  $z = 2.70 \pm 0.15$  with a (16<sup>th</sup> to 84<sup>th</sup> percentile range of  $z = 1.9\text{--}3.9$ ), which is comparable to that derived by Dudzevičiūtė et al. (2020) for AS2UDS of  $z = 2.6 \pm 0.8$  and the median redshift of the AS2COSMOS survey of  $z = 2.7 \pm 0.9$  derived by Simpson et al. (2020), as well as other studies of SMGs at similar 870  $\mu\text{m}$  flux densities (e.g. Cunha et al. 2015; Ling & Yan 2022). From the MAGPHYS SED fitting, we derive a median stellar mass for the SMGs of  $\log_{10}(M_*[\text{M}_\odot]) = 11.20 \pm 0.10$  with a 16<sup>th</sup>–84<sup>th</sup> percentile range of  $\log_{10}(M_*[\text{M}_\odot]) = 10.6\text{--}11.6$ , and a median specific star formation rate of  $\log_{10}(\text{sSFR}[\text{yr}^{-1}]) = -8.7 \pm 0.1$  with a 16<sup>th</sup>–84<sup>th</sup> percentile range of  $\log_{10}(\text{sSFR}[\text{yr}^{-1}]) = -9.2\text{--}-8.0$ . We derive a median dust mass of  $\log_{10}(M_d[\text{M}_\odot]) = 8.8 \pm 0.1$  with a 16<sup>th</sup>–84<sup>th</sup> percentile range of  $\log_{10}(M_d[\text{M}_\odot]) = 8.4\text{--}9.1$  and a median infrared luminosity of  $\log_{10}(L_{\text{IR}}[\text{L}_\odot]) = 12.6 \pm 0.1$  with a 16<sup>th</sup>–84<sup>th</sup> percentile range of  $\log_{10}(L_{\text{IR}}[\text{L}_\odot]) = 12.3\text{--}12.8$ . These are consistent with the sample of 707 SMGs

in AS2UDS, for which Dudzevičiūtė et al. (2020) derived a median stellar and dust mass of  $\log_{10}(M_*[\text{M}_\odot]) = 11.1^{+0.2}_{-0.3}$  and  $\log_{10}(M_d[\text{M}_\odot]) = 8.8^{+0.4}_{-0.4}$  and a median specific star formation rate and infrared luminosity of  $\log_{10}(\text{sSFR}[\text{yr}^{-1}]) = -8.73 \pm 0.04$  and  $\log_{10}(L_{\text{IR}}[\text{L}_\odot]) = 12.45 \pm 0.02$

As was expected, given that the JWST photometry agrees with earlier IRAC and HST observations, while typically being more sensitive, the basic derived properties of the SMGs do not change significantly when JWST photometry is included. The main benefit of deeper observations at 1–3  $\mu\text{m}$  is improved constraints on the presence of Balmer breaks at  $z \sim 1\text{--}6$ .

### 3.5. Field sample

To investigate the physical mechanism that drives and differentiates our SMG sample from the typical star-forming population at the same epochs ( $z = 2\text{--}5$ ), we compare their multi-wavelength properties to two samples of less active field galaxies. We constructed the field samples from the  $K$ -band selected sample analysed by Dudzevičiūtė et al. (2020) in the UKIDSS UDS field for which deep 22-band photometry is available covering the UV/optical through to the far-infrared/sub-millimetre and radio. Dudzevičiūtė et al. (2020) used the MAGPHYS code to derive photometric redshifts, stellar masses, and other physical properties for the  $\sim 300\,000 K_{\text{AB}} \leq 25.7$  galaxies in this  $\sim 0.8$  degree<sup>2</sup> field from the UKIDSS survey (Almaini in prep.).

Starting from this field catalogue, we first selected galaxies with no photometric flags that lie within the footprint of the JWST PRIMER survey and have estimated dust masses and far-infrared luminosities that ensure they are less actively star-forming than our SMG sample:  $M_{\text{dust}} = 10^7\text{--}10^8 \text{ M}_\odot$  and  $L_{\text{IR}} = 10^{11}\text{--}10^{12} \text{ L}_\odot$ . We then binned the redshift distribution of the SMGs and field galaxies in  $\Delta z = 0.5$  bins and in each bin we ranked the field galaxies based on their stellar masses. We then determined the number of SMGs for each bin and selected ten times as many field galaxies from the corresponding redshift

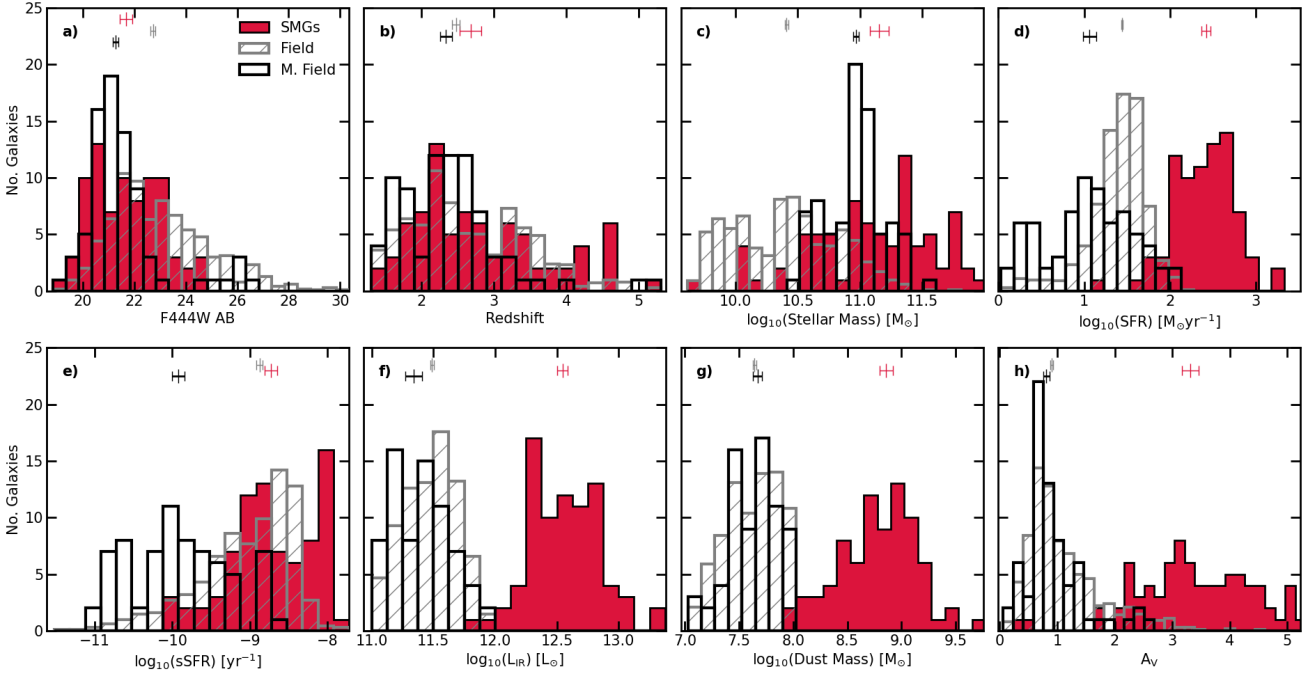


**Fig. 3.** Distributions of the magphys derived SED properties for the SMG sample (red) and field (hatched grey, scaled down by a factor of 10) and massive field (M. Field) samples (open black histograms). We show the F444W AB magnitude (a), photometric redshift (b), stellar mass (c), star formation rate (d), specific star formation rate (e), infrared luminosity (f), dust mass (g) and V-band attenuation ( $A_V$ ) (h). For each distribution, we indicate the bootstrapped median and uncertainty for SMGs (red marker and error bar) and the matched field (grey marker and error bar) and massive field sample (black marker and error bar). By construction, the less massive field sample mirrors the SMG sample in redshift and specific star formation rate distributions resulting in lower stellar masses, whilst the massive field sample more closely matches the SMGs distribution in stellar mass but with a lower median redshift. Both field samples have significantly lower dust masses, infrared luminosity, star formation rates and  $A_V$ .

bin, starting with the most massive and going down the stellar-mass ranked list. In this way, we constructed a field control sample that accurately matches the redshift distribution of our SMG sample and comprises the most massive galaxies at each epoch that have dust masses and far-infrared luminosities below those determined for the SMG population. We adopted the photometry and magphys SED fitting results from [Dudzevičiūtė et al. \(2020\)](#).

In Fig. 3, we show the distribution of physical properties for the UDS field sample in comparison to the SMGs. By construction, the field sample has similar redshift and specific star formation rates to the SMG sample, whilst having significantly lower dust masses and  $A_V$ . The field sample has a median redshift and median absolute deviation of  $z = 2.5 \pm 0.1$ , whilst their specific star formation rates are  $\text{sSFR} = -8.88 \pm 0.04 \text{ yr}^{-1}$  and  $A_V = 0.90 \pm 0.03$ . The field sample is also fainter in F444W magnitude with a median value of  $m_{\text{F444W}}^{\text{field}} = 22.74 \pm 0.10$  compared to  $m_{\text{F444W}}^{\text{SMGs}} = 21.70 \pm 0.30$ , which is reflected in the lower median stellar mass of  $\log_{10}(M_*[\text{M}_\odot]) = 10.4 \pm 0.1$ . Unfortunately, it is not possible to select a large sample of less active SFGs that are both matched to the SMG's stellar mass and redshift distributions, because most massive galaxies at  $z \geq 2-3$  are also SMGs.

To address the mass offset of the field sample, we defined a second ‘massive’ field sample. We again selected galaxies with no photometric flags lying within the PRIMER survey, but now required that they have estimated dust masses below  $M_{\text{dust}} \leq 10^8 \text{ M}_\odot$  (to ensure they are distinct from the SMGs) and stellar masses of  $M_* \geq 3.2 \times 10^{10} \text{ M}_\odot$  (to more closely match the stellar masses of the SMGs). Finally, the binned redshift distribution was used to attempt to maximise both the size of the sample and its median redshifts, while also having a comparable breadth

to the SMG redshift distribution. This resulted in a final massive field sample comprising 80 galaxies with a median stellar mass of  $\log_{10}(M_*[\text{M}_\odot]) = 11.0 \pm 0.1$ , a median far-infrared luminosity of  $\log_{10}(L_{\text{IR}}[\text{L}_\odot]) = 11.3 \pm 0.1$ , and a median redshift of  $z = 2.3 \pm 0.1$  (16–84<sup>th</sup> percentile range of  $z = 1.7$ – $2.9$ ). Hence, this second field sample is comparable in mass to the SMGs and comprises much less active SFGs, but lies at somewhat lower redshifts than the SMGs. The MAGPHYS derived SED properties of the SMGs, field and massive field samples are shown in Fig. 3.

### 3.6. Morphological analysis

In Fig. 1, we show NIRCam F277W/F356W/F444W colour images of the SMGs (ordered by decreasing 870  $\mu\text{m}$  flux), highlighting the diverse range of rest-frame optical – near-infrared morphologies from faint and red galaxies, interacting and merging systems to discs and regular spirals. These near-infrared observations sample the galaxy population at  $\leq 1 \mu\text{m}$  in the rest frame at  $\approx 1$  kpc resolution and thus provide insights into the structure and morphology of the stellar continuum emission which are much less affected by dust than previously possible.

We visually assessed as well as quantified the rest-frame near-infrared morphology of the SMGs and field galaxies using non-parametric and parametric analyses of the JWST observations. We excluded the HST observations from our morphological analysis because at the median redshift of our sample ( $z \sim 2.7$ ), HST observations only sample the rest-frame UV/optical emission of the galaxies where SMGs are inherently faint. The longer wavelength HST observations sampling the observed frame  $\approx 1.6 \mu\text{m}$  emission is also well covered by higher signal-to-noise JWST observations.

The parametric and non-parametric analysis of the JWST imaging employs  $4\farcs0 \times 4\farcs0$  cut-outs ( $\approx 30$  kpc square) of each source with a pixel scale of  $0\farcs04$  per pixel. The cut-out in each filter is centred on the source detection in the NIRCam LW (F277W+F356W+F444W) stacked image, as is detailed in Sect. 3.2. We first smoothed the source segmentation map generated from `sep` (see Sect. 3.2) using the binary dilation routine in `PHOTUTILS` (Bradley et al. 2022). Then, excluding this segmented region, we masked the remaining sources in the cut-out, down to a  $1\sigma$  isophote. This ensures full masking of any contaminants (spurious or otherwise)<sup>4</sup>. We further used `PHOTUTILS` to model (and remove) the background level in each cut-out as well as to quantify the root-mean-square (rms) noise. In the following sections, ‘cut-out’ refers to these  $4\farcs0 \times 4\farcs0$ , background-subtracted, and masked images that are used in the morphological analysis that follows.

Prior to measuring the morphology of the galaxies, we first derived the point spread function (PSF) for each of the JWST bands. We used `WEBBPSF` (version 1.2.1; Perrin et al. 2014) to generate PSF models for the MIRI and NIRCam detectors (for both short- and long-wavelength channels), which were calibrated with wavefront models at the epoch of the observations. The PSFs for each NIRCam and MIRI filter were then inserted into individual exposures of the final mosaic and drizzled to the final world co-ordinate system solution, producing a field-of-view-averaged PSF model.

### 3.6.1. Visual morphology

We first undertook a crude initial visual assessment of the morphologies of the SMGs and field samples. This involved inspection of both the colour images and `GALFIT` residual maps in the F444W band (Figs. 1 and 4) of the ALMA counterpart to identify the overall structure and any distorted morphologies, asymmetric structures, or potential tidal features. In addition, we assessed the presence of companions (either within  $\sim 1$  mag in brightness of the target galaxy, or fainter) within a wider  $10\farcs0 \times 10\farcs0$  region (out to a radius of  $\approx 40$  kpc at  $z \sim 2.7$ ). Strongly disturbed galaxies, those with tidal features or disturbed galaxies with bright companions were classed as ‘major’ mergers (M), while less disturbed galaxies or those with asymmetries and fainter companions were classed as potential ‘minor’ mergers or interacting (I) in addition to undisturbed discs (D) and compact (C) sources. These classifications are marked in Fig. 1.

### 3.6.2. Non-parametric morphology

To measure the half-light radii of the SMGs, we employ a curve of growth approach that makes no assumptions about the underlying structure of the galaxy’s light distribution. We adopt this approach because SMGs have long been assumed to originate from merger-driven events with clumpy unstable gas-rich discs, (e.g. Smail et al. 1998; Greve et al. 2005; Tacconi et al. 2008; Engel et al. 2010) and therefore the morphologies of some sources may deviate from simple parametric profiles.

We first perform a curve of growth analysis in each of the JWST bands from  $0.9 \mu\text{m}$  to  $18 \mu\text{m}$ . This is achieved by fitting a Gaussian profile to the cut-out of each galaxy to determine its image parameters, allowing the centroid ( $x, y$ ), axis ratio ( $b/a$ ) and position angle (PA) to vary. We note the original centroid of the cut-out is derived from the `sep` source detection on the

stacked F277W+F356W+F444W NIRCam bands (Sect. 3.2), and thus may not be the apparent centre of the galaxy at shorter wavelengths. A curve of growth is then derived in each band using ellipses which align to the galaxy’s axis ratio and position angle. From the curve of growth, we measure the convolved radii containing 20, 50, and 80 percent of the flux of each galaxy. The intrinsic radii of the galaxies are derived by de-convolving the sizes with the PSF in each band, measured through a similar curve of growth analysis.

To provide more quantitative, non-parametric, morphological indicators, we use the `statmorph`<sup>5</sup> code (Rodríguez-Gómez et al. 2019) which measures the Concentration, Asymmetry and Clumpiness ( $C, A, S$ ; Abraham et al. 2003; Lotz et al. 2008) parameters that quantify how concentrated, asymmetrical and clumpy the galaxies’ surface brightness profiles are, with higher values indicating more concentrated, asymmetric, or clumpier light profiles. We run `STATMORPH` on both SMG and field samples in all JWST bands using the same segmentation maps and PSFs as for the growth curve analysis described above.

In addition, the Gini and  $M_{20}$  parameters are also derived (for full definitions see Lotz et al. 2004; Snyder et al. 2015). Briefly, the Gini parameter defines the pixel distribution of the galaxy’s light, where  $G=1$  corresponds to all of the light concentrated in one pixel whilst  $G=0$  indicates each pixel contributes equally. The  $M_{20}$  parameter measures the second moment of the brightest 20 percent of pixels in the galaxy. This is normalised by the total moment for all pixels. Highly negative values indicate a high concentration of light, not necessarily at the centre of the galaxy. To validate the robustness of the `statmorph` measurements we compare the half-light radius to that derived from our curve of growth analysis. We derive a median curve of growth to `statmorph` median half-light radius ratio of  $R_{\text{h},\text{CoG}} / R_{\text{h},\text{statmorph}} = 1.06 \pm 0.01$  with a 16<sup>th</sup>–84<sup>th</sup> percentile range of  $R_{\text{h},\text{CoG}} / R_{\text{h},\text{statmorph}} = 0.93$ –1.45 for the field sample in the F444W band. This indicates good agreement between the two independent morphological measurements<sup>6</sup>.

### 3.6.3. Parametric morphology

To quantify both the parametric morphological profiles of the galaxies and the deviations from these, we used the `galfit` code (Häubler et al. 2013). `galfit` is a Python-wrapper for `galfit` (Peng et al. 2010), which allows multi-component parametric models to be fit to a galaxy’s multi-wavelength light distribution. For our analysis, we used a single Sérsic model, convolved with the PSF of the relevant JWST band. We fitted each band independently, allowing us to constrain the intrinsic wavelength dependence of the galaxy’s morphology.

To constrain the accuracy of the parametric analysis, we compare the `GALFITM` Sérsic index ( $n$ ) to that derived by `statmorph` for the field galaxies in the NIRCam F444W band. We establish a median ratio of  $n_{\text{F444W}}^{\text{GalfitM}} / n_{\text{F444W}}^{\text{statmorph}} = 1.00 \pm 0.01$  and a 16<sup>th</sup>–84<sup>th</sup> percentile range of  $n_{\text{F444W}}^{\text{GalfitM}} / n_{\text{F444W}}^{\text{statmorph}} = 0.81$ –1.26, indicating good agreement between the two independent codes.

Although a parametric Sérsic fit can model the overall distribution of a galaxy’s light profile, it is the deviations (residuals) from this simple profile – as is shown in Fig. 4 – that encode important information about the detailed structure of the

<sup>5</sup> <https://statmorph.readthedocs.io/en/latest/>

<sup>6</sup> We note however we expect some variation between the two methods due to the definitions of centroid and total fluxes used (see Lotz et al. 2004).

<sup>4</sup> We note the simultaneous modelling of nearby sources returns similar parametric results.

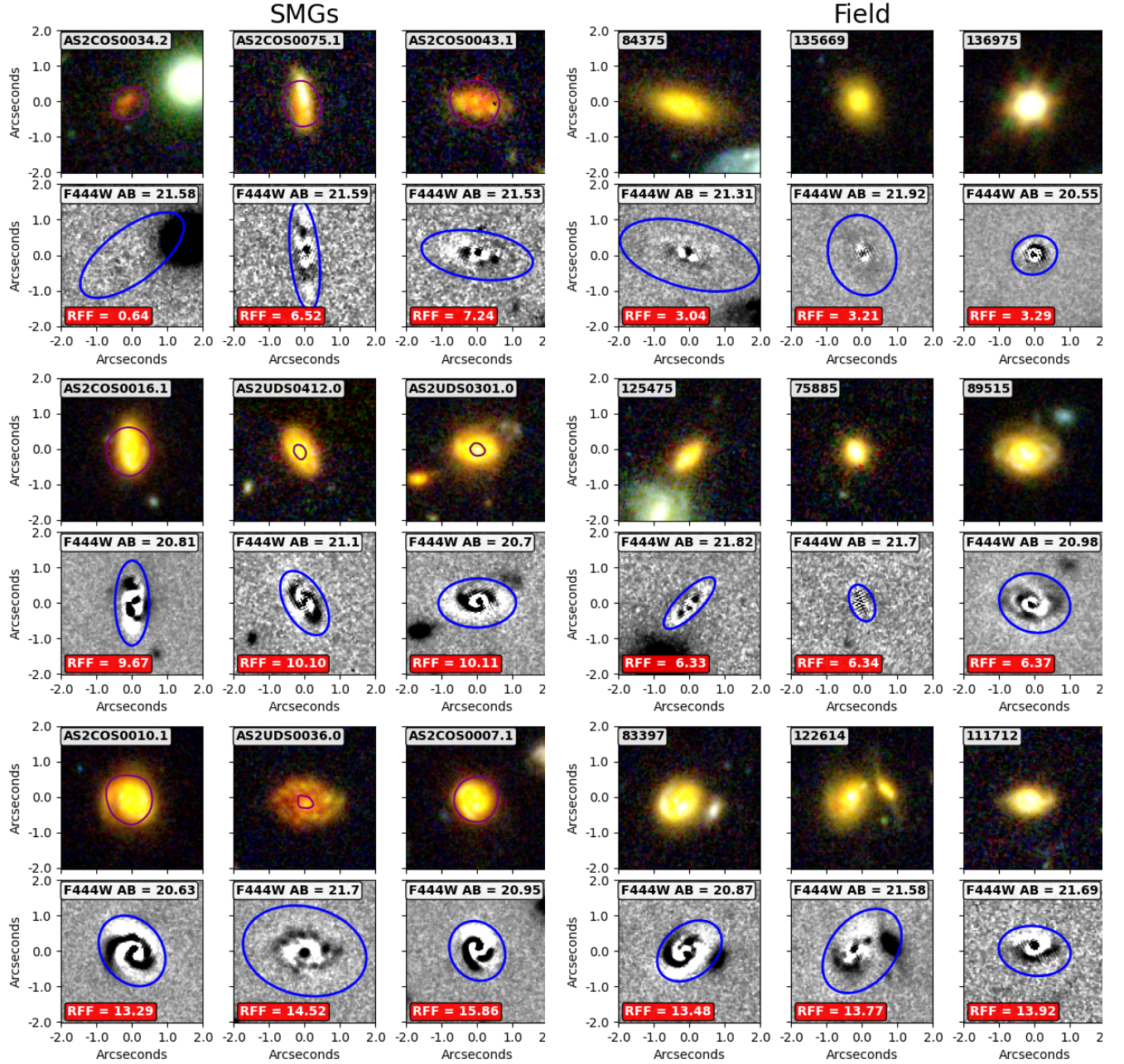


**Fig. 4.** Examples of the F356W/F277W/F115W RGB-colour image for both SMGs (*left*) and field galaxies (*right*). For the SMGs, we overlay the ALMA 870  $\mu\text{m}$   $11\sigma$  contour (purple) from Stach et al. (2019) or Simpson et al. (2020). In the lower panel of each source, we show the residuals of the GALFIT single Sérsic model fit. The blue ellipse marks the region within which we calculate the RFF of the Sérsic fit, as quantified in the lower left corner of each panel. The galaxies are selected to have a  $m_{\text{F444W}} = 20\text{--}22$  and are ranked from low-to-high RFF. No clear distinction is identified in the F444W RFF values between the SMGs and field galaxies.

galaxies. To quantify the residuals, we used the residual flux fraction (RFF) defined in Hoyos et al. (2011, 2012):

$$\text{RFF} = \frac{\sum_{i,j \in A} |I_{i,j} - I_{i,j}^{\text{model}}| - 0.8 \times \sum_{i,j \in A} \sigma_{Bkg\,i,j}}{\sum_{i,j \in A} I_{i,j}}, \quad (1)$$

where the sum was performed over all pixels within 2.5 times the Kron radius, derived in Sect. 3.2.  $|I_{i,j} - I_{i,j}^{\text{model}}|$  is the absolute value of pixel  $i,j$ 's residuals to model Sérsic model fit, whilst  $\sum_{i,j \in A} I_{i,j}$  indicates the total flux measured in the source as defined in Sect. 3.2. The 0.8 factor multiplied by the sum over the background rms of the region ( $\sigma_{Bkg\,i,j}$ ), ensures that a blank

image with constant variance has a RFF = 0.0 (for details see Hoyos et al. 2012).

It is well known that morphological codes such as `galfit` and `statmorph` systematically underestimate the uncertainties on the derived morphological parameters (e.g. Wel et al. 2012, 2024). To overcome this we employ an empirical approach which utilises the unique wavelength coverage of the NIRCam observations in the PRIMER Survey. Specifically, the majority of field galaxies (816/850) and SMGs (75/80) in our sample have both F410M and F444W observations. The F410M is a medium band filter covering the observed-frame 3.8–4.3  $\mu\text{m}$  emission, whilst the wide-band F444W filter is sensitive to the 3.8–4.9  $\mu\text{m}$

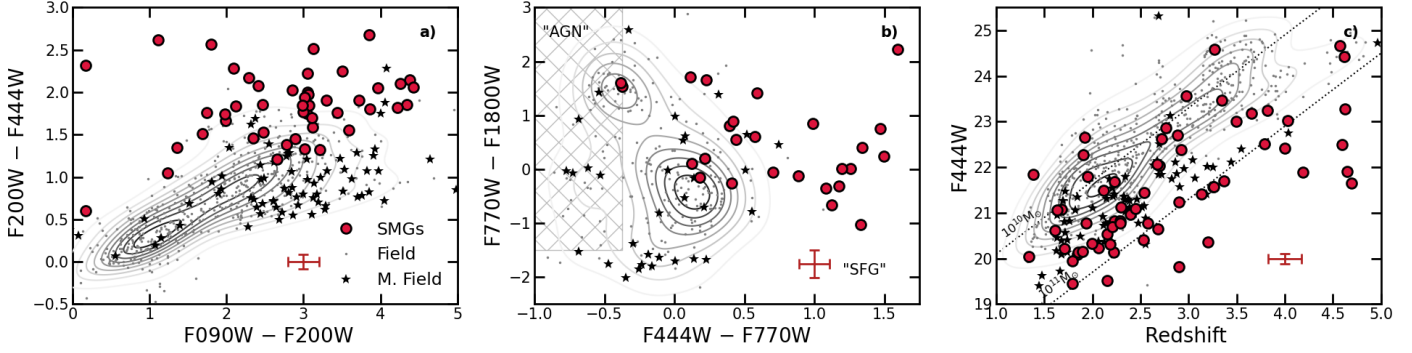


**Fig. 5.** Distribution of (a) NIRCam colours, (b) MIRI colours and (c) F444W AB magnitude as a function of redshift, with lines of constant stellar mass overlaid in the latter. A representative error bar is indicated in the lower right corner of each panel. Panel a) demonstrates the SMGs are much redder than our massive and sSFR-matched field populations, as was expected. Panel b) highlights that a fraction of SMGs and field galaxies may host AGNs with a very red F770W–F1800W colour and bluer F444W–F770W, indicating a strong upturn in the SED beyond rest-frame 3  $\mu\text{m}$ . We label the ‘AGNs’ and SFG regions in the colour space adapted from Kirkpatrick et al. (2013, 2017). We note the F770W–F1800W > 1 colour can also be driven by the 6.2  $\mu\text{m}$  PAH feature detected in the F1800W filter at  $z \sim 1.9$ . Panel c) demonstrates that the SMGs are the most massive (and so typically also brightest) galaxies at their epoch where the two field samples have been selected to be the most massive low far-infrared luminosity galaxies.

emission. Thus, for each galaxy with observations in both filters, we can make two independent measures of the galaxy’s morphology at very similar rest-frame wavelengths. Analysing the variance in morphological parameters between the two filters as a function of signal-to-noise allows us to infer a representative uncertainty on the morphological parameters at a given wavelength for each source given its signal-to-noise in that band. We use this conservative approach to quantify the uncertainties in the following analysis.

## 4. Results

From an initial sample of 88 SMGs, we have constructed a sample of 80 SMGs that are not strongly lensed and that have reliable ( $S/N > 4.5$ ) ALMA 870  $\mu\text{m}$  detections and multi-wavelength HST and JWST coverage from 0.4–18  $\mu\text{m}$ . Full details of the wavelength coverage for the individual SMGs in our sample are given in Appendix A. From the initial sample, we omitted two strongly lensed SMGs due to uncertainties on the photometry and structural properties introduced by the lensing configuration of each source, along with flagging two candidate weakly lensed sources, AS2UDS0281.0 and AS2UDS0382.0 (Fig. 1). Identifying that  $5 \pm 3\%$  of ALMA-detected SMGs in our sample are affected by foreground galaxy lensing matches the prediction of Chapman et al. (2002) that between 3 and 5 percent of sub-millimetre sources identified in blank-field SCUBA observations would be affected by lensing.

For the 60 SMGs with HST coverage, we detect no F160W counterpart at  $S/N > 3$  in 10 sources (17%). All of these have clear near-infrared counterparts in the NIRCam F444W band at  $S/N > 5$ , whilst three also have a  $S/N > 3$  in the NIRCam F150W band. This leaves seven ‘NIR-faint’ (sometimes imprecisely described as ‘HST -dark’) SMGs with no detection in the  $H$ -band ( $S/N < 3$ ). These seven SMGs have significant levels of dust attenuation as derived from MAGPHYS with  $A_V > 3.9$ . This indicates that whilst the significant dust content of these galaxies can lead to them being undetected in HST observations, it is also driven by the lack of sensitivity and depth of previous observations.

Of the 78 SMGs with NIRCam short-wavelength (SW) coverage, we identify one galaxy, AS2UDS0346.0 at  $z = 4.1$ , that is undetected ( $S/N < 3$ ) bluewards of 2.7  $\mu\text{m}$ , and first detected by

JWST in the F277W band at  $S/N \geq 5$ . From our MAGPHYS analysis we derive significant dust attenuation with  $A_V = 5.1_{-0.6}^{+2.0}$  for AS2UDS0346.0 with a stellar mass of  $\log_{10}(M_*/[\text{M}_\odot]) = 11.2_{-0.2}^{+0.1}$  that is representative of our sample. For SMGs with suitable NIRCam coverage we identify detections ( $S/N > 3$ ) in F200W for 96% (70/73), in F150W for 87% (68/78) and in F090W for 59% (43/73) of the sources, respectively. All have  $S/N > 3$  detections in the NIRCam-LW and MIRI bands.

In Fig. 5 we investigate the photometric properties of the SMGs in the JWST bands by comparing the NIRCam and MIRI colours. Specifically, in Fig. 5a we compare the NIRCam F200W–F444W colour with the F090W–F200W colour. At the median redshift of the SMG and field galaxies, these filters sample the rest-frame  $UVJ$  regime of the galaxies’ spectral energy distributions, highlighting the distinct red nature of the SMGs compared to the general field. Given this, it may be possible by colour selection to identify the JWST counterpart to the submillimetre bright SCUBA-2 source without requiring higher resolution ALMA observations (e.g. Alberts et al. 2013; Chen et al. 2016; An et al. 2018; Hwang et al. 2021). To investigate this, for each SMG we compare the NIRCam F200W–F444W colour of all sources detected in the 14''.8 diameter SCUBA-2 beam to that of the ALMA-selected SMG. However only in 51% (41/80) of the SCUBA-2 observations, the ALMA source represents the reddest source in the beam. This indicates that whilst colour is a good identifier of SMGs, further information such as proximity to source centroid, predicted 870  $\mu\text{m}$  fluxes and multi-wavelength observations from infrared to radio are required to isolate the exact near-infrared counterpart (e.g. Downes et al. 1986; Ivison et al. 2002; Hodge et al. 2013; Casey et al. 2013; An et al. 2018; Gillman et al. 2023).

Figure 5b compares the MIRI and NIRCam colours with the F770W–F1800W colour shown as a function of F444W–F770W colour. At the median redshift of the SMG and field galaxies, these filters sample the rest-frame near and mid-infrared. The SMGs on average have redder F444W–F770W colours with comparable F770W–F1800W colours to the field population, reflecting the dust attenuation of the shorter wavelength light. The SMGs and field galaxies which exhibit very red F770W–F1800W colours with bluer F444W–F770W colour may indicate the presence of active galactic nuclei (AGNs), as was noted by Ivison et al. (2004) who used MIPS/24  $\mu\text{m}$

and IRAC colours to identify AGNs and starburst galaxies. We highlight the regions of the colour diagram that an ‘AGN’ or SFG would likely inhabit, adapted from Kirkpatrick et al. (2013, 2017). Of those with MIRI coverage, we identify  $24 \pm 5\%$  (69/282) of the field galaxies (and  $21 \pm 3\%$  (7/33) of the massive field sample) have near-infrared colours that may indicate the presence of AGN activity whilst for the SMGs we derive a lower fraction of  $3 \pm 1\%$  (2/37). The two SMGs with AGN-like colours, AS2UDS0259.0 and AS2UDS0659.0, both exhibit extended morphologies in the MIRI F770W and F1800W observations with no visible point source, indicating any contribution from an AGN is minimal. This is in agreement with previous studies which identify the AGN contribution in SMGs to be small (e.g. Stach et al. 2019). There are four SMGs with a compact, point-source like morphology. AS2UDS0173.0 which is not covered by the MIRI observations as well as AS2UDS287.1, AS2UDS509.0 and AS2UDS516.0. All sources appear point-source like in all JWST bands, suggesting they may just be compact galaxies, as is indicated in Fig. 1. The SFG and AGN classification in Fig. 5b does not fully encapsulate the bi-modality present in the colour space, especially in the field galaxies. Galaxies with  $F1800W - F770W > 1$  and  $F444W - F770W < 0$ , represent a bright ( $m_{F444W} = 21.5 \pm 0.1$ ) lower redshift subset ( $z = 1.9 \pm 0.04$ ) with significantly brighter F1800W emission ( $m_{F1800W} = 20.3 \pm 0.1$ ) compared to the ‘bluer’ population ( $z = 2.9 \pm 0.1$ ,  $m_{F444W} = 22.9 \pm 0.1$ ,  $m_{F1800W} = 23.3 \pm 0.1$ ). At  $z = 1.9$ , the F1800W filter is sensitive to the  $6.2 \mu\text{m}$  PAH feature, which can strongly enhance the mid-infrared emission in massive galaxies, resulting in red F770W–F1800W colours (e.g. Draine et al. 2007; Aniano et al. 2020; Shvaei et al. 2024).

In Fig. 5c we show the correlation between NIRCam F444W magnitude and the redshift of the galaxies. We overlay lines of constant stellar mass, highlighting that the SMGs are the most massive galaxies at their epoch (Dudzevičiūtė et al. 2020), the massive field sample being comparable and the less massive field sample exhibiting lower stellar masses at all epochs.

#### 4.1. Near-infrared morphology

While SMGs have long been known to exhibit complex, potentially merger-like, morphologies based on rest frame *UV* imaging (e.g. Smail et al. 1998; Chapman et al. 2004; Swinbank et al. 2010; Aguirre et al. 2013) the influence of dust has meant their true stellar morphologies are still unknown. The combination of near-infrared colour images (Fig. 1) and F444W Sérsic fit residual maps (Fig. 4) provides an unprecedented insight into the stellar structures and asymmetries in the SMGs.

From a visual inspection, in 21/80 SMGs, we identify clear spiral arm features in the Sérsic model residuals, as well as clear clumpy structures in  $30 \pm 4\%$  (24/80) of the SMGs. In particular, one galaxy AS2UDS0259.0, shows a bar-like structure in the F444W image indicating complex stellar structures may be present, similar to those identified in recent JWST and ALMA studies (e.g. Hodge et al. 2019; Smail et al. 2023; Rujopakarn et al. 2023; Liu et al. 2023).

We estimate that  $40 \pm 10\%$  (32/80) of the SMGs are isolated systems, with no strong perturbations or obvious bright neighbours on  $\simeq 20\text{--}30 \text{ kpc}$  (projected) scales, while 16 SMGs ( $20 \pm 5\%$ ) in our sample have potential companions or are interacting with another massive galaxy suggesting major mergers, the remaining 32 SMGs ( $40 \pm 10\%$ ) have faint companions and show signs of disturbance (e.g. asymmetries in the GALFIT F444W residuals) that suggest potential minor interactions and mergers. There are at least two such examples in

our sample of SCUBA-2 sources, S2UDS0322 and S2COS0034, and one ALMA source (AS2UDS0071.0) that comprise multiple ALMA-detected, or NIRCam-F444W detected, galaxies that show clear signs of galaxy interactions with S2COS0034 comprising two SMGs that are both detected in [CII] emission at  $z_{[\text{CII}]} = 4.62$  (Mitsuhashi et al. 2021).

The median far-infrared luminosity of the candidate major mergers is  $L_{\text{IR}} = 10^{12.53 \pm 0.05} L_{\odot}$ , compared to  $L_{\text{IR}} = 10^{12.49 \pm 0.05} L_{\odot}$  for the remainder of the sample, indicating no strong dependence of far-infrared luminosity on merger state (e.g. Hopkins et al. 2010). Indeed, an equivalent visual classification of the less active field sample returns very similar merger statistics with  $25 \pm 5\%$  of the sample showing evidence for potential major mergers and the remaining  $\sim 75\%$  showing much weaker or no evidence for merger-related disturbance or companions on  $\simeq 20\text{--}30 \text{ kpc}$  scales. This similarity in the rate of mergers between SMGs and less active galaxies is consistent with the theoretical results from the EAGLE simulation from McAlpine et al. (2019) who found that simulated SMGs had similar rates of recent mergers to less active galaxies, in part because most galaxies at high redshifts are undergoing continuous infall and merging.

To summarise, while signs of potential dynamical disturbance are frequently seen in our SMG sample, we conclude that the majority of SMGs do not appear to be the result of late-stage, major mergers. This is in contrast with the situation for similar far-infrared luminous populations at  $z \sim 0$ , where systems with far-infrared luminosities of  $L_{\text{IR}} \geq 10^{12} L_{\odot}$  are frequently associated with late-stage major mergers (e.g. Sanders et al. 1988; Farrah et al. 2001), although there are claims that this fraction declines at  $z \sim 1$  (e.g. Kartaltepe et al. 2010), with an increasing fraction of starburst galaxies appearing to be isolated systems (e.g. Faisst et al. 2024). It is also in contrast to early studies of SMGs with resolved CO kinematics (e.g. Engel et al. 2010) as well near-infrared spectroscopic observations (e.g. Alaghband-Zadeh et al. 2012; Drew et al. 2020) which suggested that the majority of SMGs are mergers, with distinct separated dust-detected components.

##### 4.1.1. Sizes, Sérsic indices, and axis ratios

We measure the half-light radius of the SMGs and field galaxies in the F444W band, determining median values of  $R_h^{\text{SMG}} = 2.70 \pm 0.23 \text{ kpc}$  and  $R_h^{\text{field}} = 2.50 \pm 0.10 \text{ kpc}$  with 16<sup>th</sup>–84<sup>th</sup> percentile ranges of  $R_h^{\text{SMG}} = 1.82\text{--}4.36 \text{ kpc}$  and  $R_h^{\text{field}} = 1.64\text{--}3.76 \text{ kpc}$ , respectively. For the massive field sample, we determine a median of  $R_h^{\text{M. field}} = 2.42 \pm 0.15 \text{ kpc}$  with a 16<sup>th</sup>–84<sup>th</sup> percentile range of  $R_h^{\text{M. field}} = 1.70\text{--}3.47 \text{ kpc}$ . This is comparable to the rest-frame  $1.5 \mu\text{m}$  size measured by Martorano et al. (2024) for massive  $\log_{10}(M_*/[M_{\odot}]) = 11.0\text{--}11.5$  SFGs at  $2.0 \leq z \leq 2.5$  with a median size of  $R_h^{1.5 \mu\text{m}} = 2.24 \text{ kpc}$  with a 16<sup>th</sup>–84<sup>th</sup> percentile range of  $R_h^{1.5 \mu\text{m}} = 1.55\text{--}4.27 \text{ kpc}$ .

To establish whether the SMGs and field galaxies are drawn from the same underlying distribution, we perform a Kolmogorov-Smirnov (KS) test on the mass normalised distributions of half-light radius. To mass normalise the half-light radius distributions, we adopt the rest-frame optical mass-size relation from Ward et al. (2024) at  $2 < z < 3$ , noting that this is consistent with the trends seen in our samples. From the median stellar mass of the less active field galaxies to the median stellar mass of the SMG sample, we derive an increase in half-light radius of  $27 \pm 6\%$ , which we apply to the less massive field galaxies’ half-light radii to account for the offset in stellar mass between the two samples. For the massive field

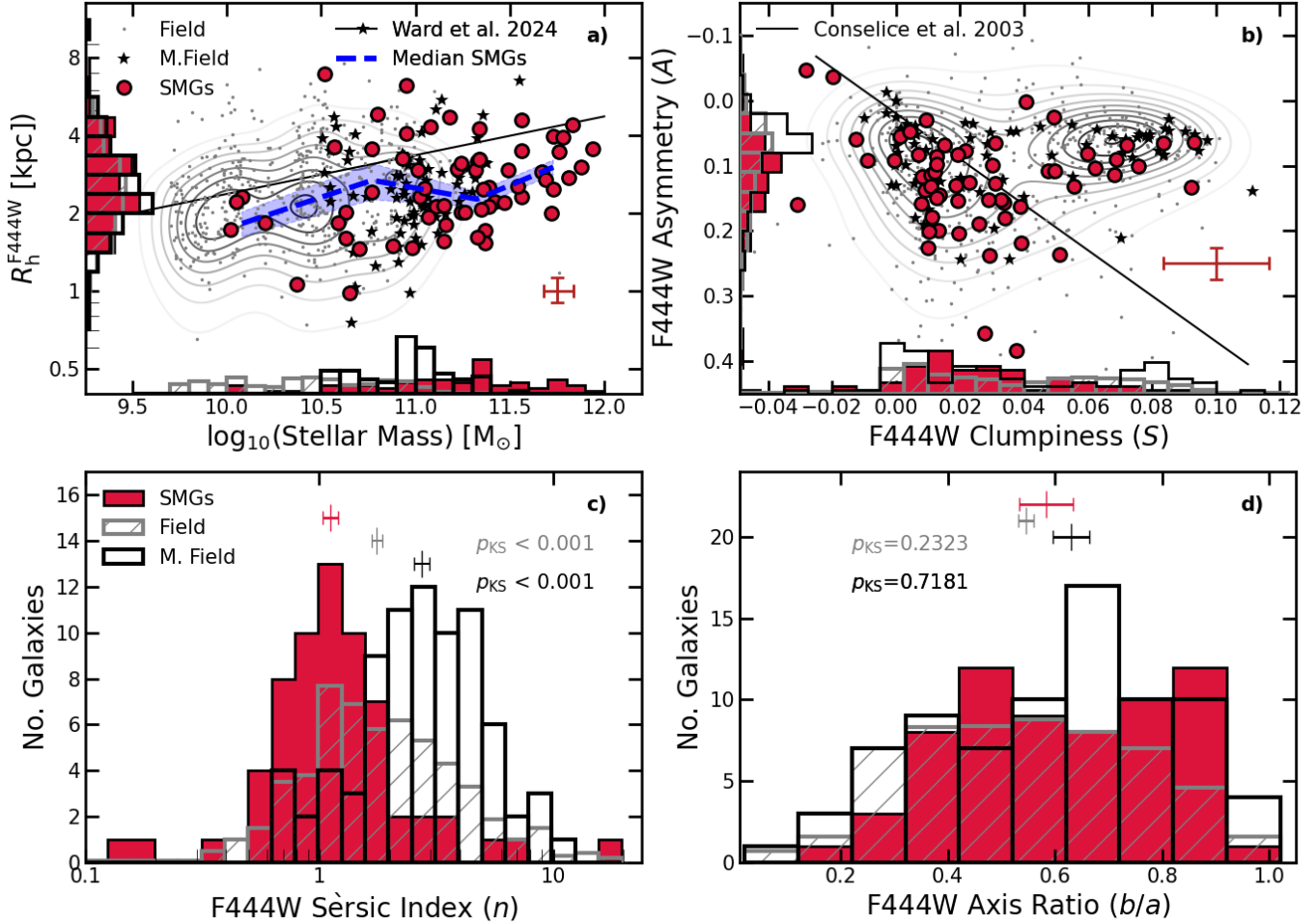


**Fig. 6.** Correlation between *a*) stellar mass and half-light radius, and *b*) the Clumpiness ( $S$ ) and Asymmetry ( $A$ ) for the SMG and field samples in the NIRCam F444W filter. In each panel we show histograms of each parameter for the field (hatched grey histogram, scaled down by a factor 10), massive field (black) and SMG sample (red). In panel *a*) we also overlay the mass-size relation for  $2 < z < 3$  SFGs from Ward et al. (2024) and in panel *b*) the relation between Asymmetry and Clumpiness identified by Conselice et al. (2003). In panels *c*) and *d*) we show the distributions of Sérsic index ( $n$ ) and axis ratio ( $b/a$ ) in the F444W band. For each distribution, we display the KS probability ( $p_{\text{KS}}$ ) that each field sample and the SMG distributions are drawn from the same parent population, where  $p_{\text{KS}} < 0.001$  suggests a significant difference in the distributions. We plot the bootstrap median and uncertainty for the two distributions at the top of each panel. The SMGs, on average, have comparable sizes and lower Sérsic indexes than both field samples, whilst exhibiting similar axis ratios and clumpiness with higher asymmetry.

sample we make a direct comparison to the SMGs. For the non-Gaussian distributions of SMG and field galaxy morphological properties, we require  $p_{\text{KS}} \leq 0.003$  ( $>3\sigma$ ) to confirm the populations are inherently different. We conclude the SMGs and both field galaxy samples have indistinguishable distributions of mass normalised half-light radius with  $p_{\text{KS}} = 0.06$  for the less massive field sample and  $p_{\text{KS}} = 0.36$  for the massive field sample.

In Fig. 6a we show the correlation between stellar mass and F444W half-light radius for both field samples and the SMGs. We overlay the rest-frame optical mass-size relation for SFGs at  $2 < z < 3$  from Ward et al. (2024). On average, the field galaxies follow the trend identified by Ward et al. (2024), whilst the SMGs, as is indicated by the running median in Fig. 6a, exhibit marginally smaller F444W sizes for stellar masses above  $\log_{10}(M_*/[M_\odot]) > 10.5$ . We note however that the majority of galaxies used to define the mass-size relation in Ward et al. (2024) have a stellar mass of  $\log_{10}(M_*/[M_\odot]) < 10.5$ . In panel *c*) of Fig. 6, we compare the distribution Sérsic index for the field sample to those of the SMGs, identifying more disc-like Sérsic indices for the SMGs with a median of  $n_{\text{F444W}} = 1.10 \pm 0.10$

and a 16<sup>th</sup>–84<sup>th</sup> percentile range of  $n_{\text{F444W}} = 0.63$ –1.98 whilst the lower mass field galaxies have a higher median value of  $n_{\text{F444W}} = 1.85 \pm 0.07$  with a 16<sup>th</sup>–84<sup>th</sup> percentile range of  $n_{\text{F444W}} = 0.88$ –4.35. The massive field sample has an even higher median Sérsic index of  $n_{\text{F444W}} = 2.78 \pm 0.20$  and a 16<sup>th</sup>–84<sup>th</sup> percentile range of  $n_{\text{F444W}} = 1.51$ –4.89. Applying a KS test, we identify that the SMGs are distinct compared to either the field or the massive field distributions with  $p_{\text{KS}} < 0.001$  for both<sup>7</sup>.

From our non-parametric analysis, we derive a median axis ratio of  $b/a = 0.55 \pm 0.03$  for the SMGs and a 16<sup>th</sup>–84<sup>th</sup> percentile range of  $b/a = 0.37$ –0.82 in the NIRCam F444W band. This is comparable to the axis ratio distribution for 870  $\mu\text{m}$  dust continuum in SMGs with  $b/a = 0.63 \pm 0.02$  (Gullberg et al. 2019). For the field galaxies, we derive a median F444W axis ratio of  $b/a = 0.53 \pm 0.01$  and 16<sup>th</sup>–84<sup>th</sup> percentile range  $b/a = 0.31$ –0.77, whilst for the massive field sample we derive a median  $b/a = 0.64 \pm 0.03$  and 16<sup>th</sup>–84<sup>th</sup> percentile range  $b/a = 0.35$ –0.84. The distribution of axis ratios, as is shown in

<sup>7</sup> We note that the exclusion of the candidate mergers does not affect this result.

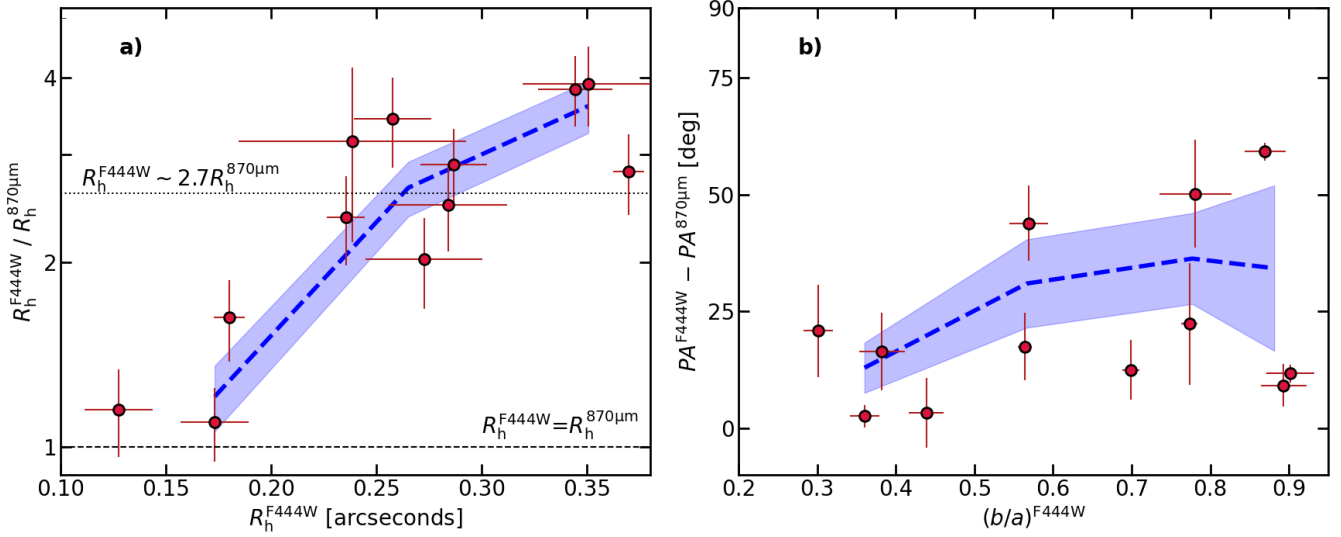


**Fig. 7.** Comparison of the ALMA 870  $\mu\text{m}$  morphological properties to the NIRCam F444W morphologies for the subset of SMGs with high-resolution ALMA observations from Gullberg et al. (2019). We compare (a) the half-light radii and (b) the position angle as a function of axis ratio, with a running median (blue line and shaded region) shown in each panel. On average we identify significantly smaller 870  $\mu\text{m}$  sizes ( $R_h^{\text{F444W}} / R_h^{870\mu\text{m}} = 2.7 \pm 0.4$ ) but consistent axis ratios ( $b/a_{\text{F444W}} / b/a_{870\mu\text{m}} = 0.95 \pm 0.11$ ) and position angles ( $\text{PA}_{\text{F444W}} - \text{PA}_{870\mu\text{m}} = 17 \pm 5^\circ$ ), with a larger offset in position towards more circular axis ratios where the position angle is more degenerate.

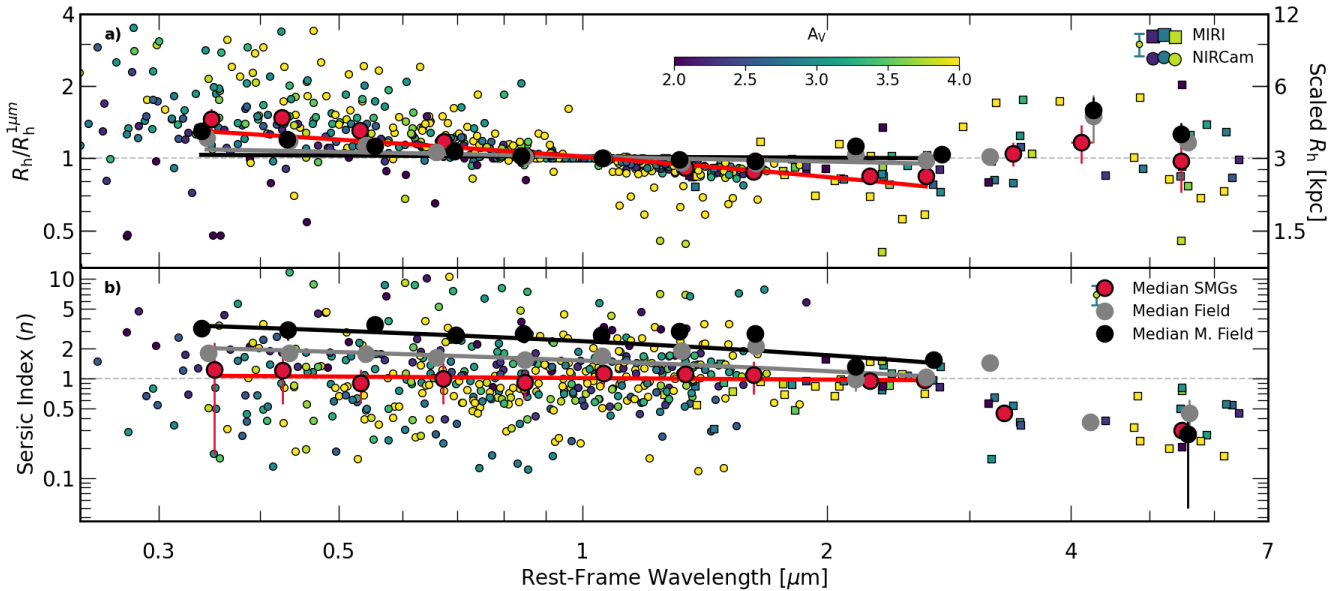


**Fig. 8.** Morphology of SMGs and field galaxies as a function of wavelength. a) The growth curve half-light radius ( $R_h$ ) of the SMGs, normalised by the rest-frame 1  $\mu\text{m}$  half-light radius of the respective galaxy as a function of rest-frame wavelength and colour-coded by the galaxy integrated  $A_V$ . We show individual measurements for SMGs, and a representative error bar, as well as the running median for the field sample (grey points and line) and massive field sample (black points and line). On the right-hand axis we show the normalised half-light radius scaled by the median rest-frame 1  $\mu\text{m}$  size ( $R_h^{1\mu\text{m}} = 3.1 \text{ kpc}$ ) for the SMGs. b) Sérsic index derived from the `galfit` parametric fitting as a function of rest-frame wavelength. We indicate the NIRCam measurements by circles and MIRI measurements by squares. We show a running median, and standard error ( $\sigma / \sqrt{n}$ ) in fixed logarithmic bins of wavelength for the SMGs and field galaxies. In both panels, we plot the parametric fit for the field (solid grey line) and SMGs (solid red line). We find that the SMGs, on average, have a stronger size variation with wavelength, becoming more compact at longer wavelengths quicker than either field sample, whilst exhibiting lower Sérsic index at all wavelengths.

Fig. 6d, is comparable to that of the SMGs with  $p_{\text{KS}} = 0.23$  for the field sample and  $p_{\text{KS}} = 0.72$  for the massive field sample.

#### 4.1.2. Residuals, clumpiness, and asymmetry

Whilst the Sérsic profiles indicate more disc-like surface brightness distributions in F444W for the SMGs, it is the deviations

from the parametric light profiles, quantified by the RFF parameter, which encode the detailed morphological properties of each galaxy. In Fig. 4 we show examples of the NIRCam F444W Sérsic model residuals, and the derived RFF values, for both SMGs and field galaxies. Whilst some galaxies exhibit smooth residuals, and low RFF values, several galaxies (both SMGs and field) display complex morphologies with multiple clumps, spiral arms

or bright compact point sources. For the SMGs we identify a median RFF value in the F444W band of  $RFF^{F444W} = 10.2 \pm 0.5$  with a 16<sup>th</sup>–84<sup>th</sup> percentile range of  $RFF^{F444W} = 5.9$ –16.3 whilst the field galaxies have a median value of  $RFF^{F444W} = 8.5 \pm 0.2$  with a 16<sup>th</sup>–84<sup>th</sup> percentile range of  $RFF^{F444W} = 4.5$ –17.2. The massive field galaxies have a median RFF value in the F444W band of  $RFF^{F444W} = 7.0 \pm 0.63$  with a 16<sup>th</sup>–84<sup>th</sup> percentile range of  $RFF^{F444W} = 4.4$ –11.85. We compare the distributions of RFF for SMGs and field samples finding a KS-statistic of  $p_{KS} = 0.002$  for the lower mass field sample, and  $p_{KS} < 0.001$  for the high-mass field. This indicates that the larger, less massive, field sample is not distinguishable at  $>3\sigma$  level to the SMGs, whilst the massive field sample, with lower RFF values, is distinct from the SMGs.

Although the 870  $\mu\text{m}$  ALMA observations of the majority of the SMGs in our sample are not high enough resolution ( $\text{FWHM} \leq 0''.2$ ) to identify these structural features, high-resolution sub-millimetre studies have identified spiral arms, bars and star-forming rings embedded in exponential dust discs (e.g. Hodge et al. 2019; Amvrosiadis et al. 2024). For a subset of the SMGs (15/80), however, 0''.2 resolution ALMA 870  $\mu\text{m}$  observations are available, as is discussed by Gullberg et al. (2019). These resolved observations are insufficient to identify complex dust structures, but the resolved 870  $\mu\text{m}$  emission's morphology provides insight into any underlying structural features. For these 15 SMGs we first compare the ALMA 870  $\mu\text{m}$  size measured in the  $uv$  plane to the F444W growth curve size, as is shown in Fig. 7a. We estimate a median ratio of  $R_h^{F444W} / R_h^{870\,\mu\text{m}} = 2.7 \pm 0.4$  with a 16<sup>th</sup>–84<sup>th</sup> range of  $R_h^{F444W} / R_h^{870\,\mu\text{m}} = 1.5$ –3.5. As identified by previous studies the far-infrared emission is much more compact than the stellar emission at shorter wavelengths (e.g. Simpson et al. 2015; Lang et al. 2019; Gullberg et al. 2019; Chen et al. 2022). We perform a Spearman rank test on the correlation between F444W/870  $\mu\text{m}$  size ratio and the  $A_V$  of the galaxy, identifying no significant correlation ( $p_{SR} = 0.33$ ). However, a larger sample is required to robustly confirm the lack of correlation.

To investigate the presence of complex dust structures we compare the 870  $\mu\text{m}$  axis ratio and position angle to that derived for the F444W emission. For the 870  $\mu\text{m}$  emission we adopt the free Sérsic fitting parameters from Gullberg et al. (2019). We identify median ratios of  $b/a_{F444W} / b/a_{870\,\mu\text{m}} = 0.95 \pm 0.11$  and, as is shown in Fig. 7b, a median offset in axis ratio of  $\text{PA}_{F444W} - \text{PA}_{870\,\mu\text{m}} = 17 \pm 5^\circ$ , indicating good agreement in the alignment of the near-infrared (rest-frame  $\approx 1\,\mu\text{m}$ ) and far-infrared (rest-frame  $\approx 250\,\mu\text{m}$ ) emission, suggesting they are tracing the same underlying structure, in contrast to the UV/optical and far-infrared offsets identified in previous multi-wavelength high-resolution studies (e.g. Chen et al. 2015; Calistro Rivera et al. 2018; Hodge et al. 2019).

In Fig. 6b we show the correlation between asymmetry ( $A$ ) and clumpiness ( $S$ ) in the NIRCam F444W band as derived from statmorph and over plot the relation between  $A$  and  $S$  derived by Conselice et al. (2003)<sup>8</sup>. We find that the SMGs and field galaxies have similar clumpiness with a median value of  $S^{\text{SMGs}}_{F444W} = 0.02^{+0.03}_{-0.02}$  and  $S^{\text{field}}_{F444W} = 0.03^{+0.04}_{-0.04}$ , respectively with a  $p_{KS} = 0.02$ . The massive field sample has  $S^{\text{M,field}}_{F444W} = 0.03^{+0.05}_{-0.01}$ , with a  $p_{KS} = 0.01$ . This indicates that both field and massive field samples are broadly consistent with being drawn from similar distributions to the SMGs. The asymmetry in the F444W band for the SMGs is higher with a median

value of  $A^{\text{SMGs}}_{F444W} = 0.13^{+0.09}_{-0.06}$  compared to the field galaxies ( $A^{\text{field}}_{F444W} = 0.08^{+0.12}_{-0.06}$ ) and a  $p_{KS} < 0.001$ . The massive field sample has median value of  $A^{\text{M,field}}_{F444W} = 0.07^{+0.06}_{-0.03}$  with a  $p_{KS} < 0.001$  indicating the field galaxies and massive field galaxies asymmetry distributions are distinct from the SMGs.

The correlation between asymmetry and clumpiness highlights two distinct regions. At constant asymmetry, there are two populations, one at low clumpiness ( $S < 0.04$ ) and one at high clumpiness ( $S > 0.04$ ), where the majority of the SMGs and field galaxies have low clumpiness with smooth, symmetric light distributions whilst those galaxies at high clumpiness show signs of concentrated star-forming regions. The SMGs at  $S > 0.04$  are more compact in the F444W filter with a median size of  $R_h = 1.72 \pm 0.14$  kpc compared to the SMGs with lower clumpiness ( $S < 0.04$ ) with a median size of  $R_h = 2.96 \pm 0.25$  kpc, whilst exhibiting comparable morphological and MAGPHYS derived properties. We note that several studies have highlighted the uncertainty introduced in non-parametric morphological measurements when the Petrosian radius of the galaxy ( $R_p$ ) is comparable to the HWHM of the observations (e.g. Yu et al. 2023; Ren et al. 2024), especially when the clumpiness parameter is measured between  $0.25R_p$  and  $1.5R_p$ , see Lotz et al. (2004) for details. This suggests that the non-parametric measurements for these compact galaxies maybe more uncertain than for the more extended sources.

## 4.2. Wavelength-dependent morphology

The preceding analysis of the SMGs and field galaxies stellar (near-infrared) morphologies has revealed broad similarities between the two populations. Many previous studies suggest the extreme properties of SMGs originate from merger-driven events (e.g. Smail et al. 1998; Swinbank et al. 2010; Aguirre et al. 2013). We do not expect the morphological signatures of these mergers to show wavelength dependence in contrast to the effects of dust. Thus, by quantifying the morphological variation with wavelength in the field and SMG sample, we can test the applicability of the merger-driven scenario.

For the SMGs and field galaxies we measure a median F200W half-light radii of  $R_{h,F200W}^{\text{SMG}} = 4.0 \pm 0.3$  kpc and  $R_{h,F200W}^{\text{field}} = 2.8 \pm 0.1$  kpc, respectively. Compared to F444W, for the SMGs this represents a  $48 \pm 0.17\%$  reduction in size between 2  $\mu\text{m}$  and 4  $\mu\text{m}$ , whilst for the field galaxies the reduction in size is only  $12 \pm 6\%$ , although we note this comparison is not done at fixed stellar mass it highlights the variation of morphology with wavelength for the two samples. The massive field sample has a median F200W half-light radii of  $R_{h,F200W}^{\text{M,field}} = 2.9 \pm 0.2$  kpc which corresponds to a  $20 \pm 11\%$  reduction in size. To further investigate the variation in the SMGs and field galaxy morphology as a function of wavelength, in Fig. 8 we plot the half-light radius, normalised by the rest-frame 1  $\mu\text{m}$  half-light radius, and Sérsic index against the rest-frame wavelength probed by the NIRCam and MIRI observations.

Below 1  $\mu\text{m}$ , for SMGs in Fig. 8 there is increased spread in half-light radius with an apparent correlation with dust content as quantified by  $A_V$ . At rest-frame wavelengths greater than 3  $\mu\text{m}$ , where we use the MIRI F770W and F1800W bands to quantify the morphology, we identify a decrease in the median Sérsic index of both field and SMGs to  $n \sim 0.4$  and an increase in the half-light radius. We suspect that this trend is driven by the larger beam size of the MIRI observations with  $\text{FWHM} = 0''.27$  and  $0''.59$ , respectively for the F770W and F1800W filters, in combination with the shallower depth compared to the NIRCam

<sup>8</sup> The relation is corrected for the different definitions of clumpiness given by Lotz et al. (2004) and Conselice et al. (2003).

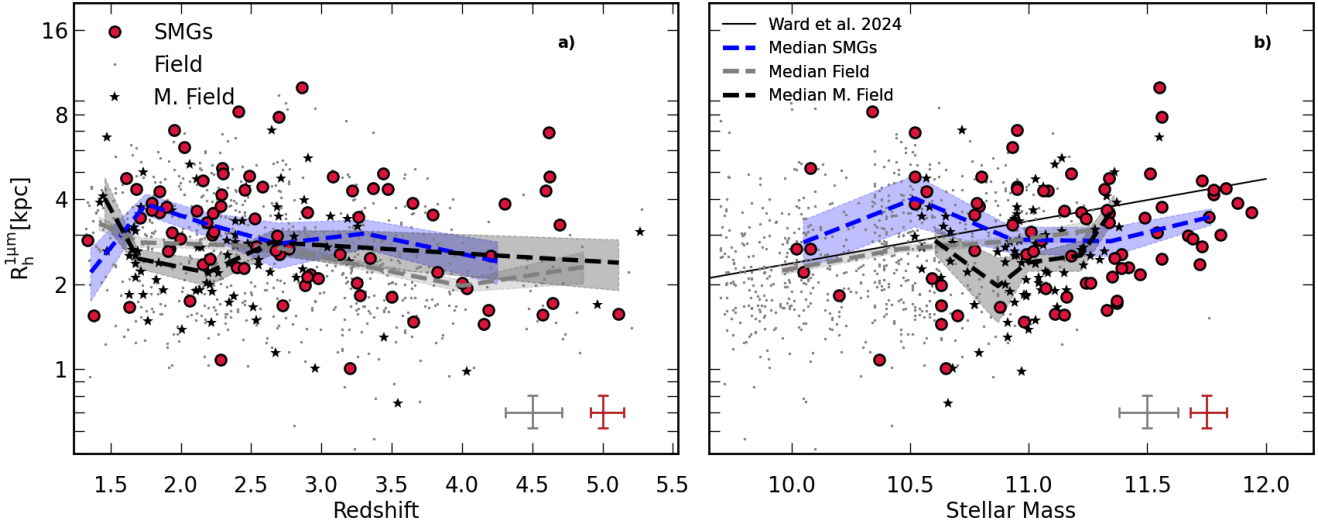


**Fig. 9.** Rest-frame 1  $\mu\text{m}$  half-light radius for SMGs (red circles), less massive field galaxies (grey dots) and massive field galaxies (black stars) as a function of (a) redshift and (b) stellar mass. In each panel, we show a running median for SMGs (dashed blue line), field galaxies (dashed grey line) and massive field galaxies (dashed black line) as well as a representative uncertainty. We identify a consistent reduction in rest-frame 1  $\mu\text{m}$  size with increasing redshift in both field samples and the SMG sample, as well as a consistent mass-size relation compared to that seen in Fig. 6. This indicates that the morphology variation with wavelength identified in both field samples and the SMGs in Fig. 8 is not driven by K-correction effects.

observations, resulting in a smoother, less structured, light distribution. In addition, in the rest-frame near-infrared ( $>3 \mu\text{m}$ ) any AGN component that is present in the galaxy starts to be more prominent over the stellar emission, with point-source ( $n \sim 0.5$ ) morphology.

To quantify the field galaxy and SMGs size evolution with wavelength, we perform fits to the median values shown in Fig. 8 up to rest-frame 3  $\mu\text{m}$  using an orthogonal distance relation (ODR) algorithm that takes into account the uncertainties on the median values in both wavelength and size. We define the function as

$$\frac{R(\lambda)}{R_{1\mu\text{m}}} = \frac{d(R_h/R_{1\mu\text{m}})}{d\lambda} \log_{10}(\lambda), \quad (2)$$

where  $\lambda$  is the rest-frame wavelength probed by the observations. For the SMGs we derive a slope of  $\frac{d(R_h/R_{1\mu\text{m}})}{d\lambda} = -0.60 \pm 0.09$  whilst for the field galaxies we estimate  $\frac{d(R_h/R_{1\mu\text{m}})}{d\lambda} = -0.15 \pm 0.07$  and the massive field galaxies  $\frac{d(R_h/R_{1\mu\text{m}})}{d\lambda} = -0.04 \pm 0.09$ . This indicates the SMGs have stronger variation in size with wavelength, becoming more compact faster than either field sample, as highlighted by the best-fit solution plotted in Fig. 8. However, this trend may be driven by centrally concentrated dust inflating the rest-frame optical sizes of the SMGs resulting in a stronger observed variation with wavelength. To ensure size ( $R_h$ ) variation with wavelength identified in the SMGs and field galaxies in Fig. 8 is not driven by the redshift evolution of the galaxies, in Fig. 9, we correlate the rest-frame 1  $\mu\text{m}$  size of the galaxies with their redshift. On average we identify a consistent redshift evolution in the near-infrared sizes of the SMGs and both field samples, indicating that redshift dependent K-corrections are not driving the morphological wavelength variation.

Furthermore Fig. 8 shows that the SMGs, on average, have a lower Sérsic index than the field galaxies at all wavelengths. To quantify the evolution of Sérsic index with wavelength we fit a similar relation to that used to quantify the size evolution of the

form

$$n(\lambda) = n_0 + \frac{dn}{d\lambda} \log_{10}(\lambda), \quad (3)$$

up to a rest-frame wavelength of 3  $\mu\text{m}$ . The median Sérsic index of the SMGs have an  $\frac{dn}{d\lambda} = -0.12 \pm 0.11$  and  $n_0 = 1.00 \pm 0.04$ , whilst the field galaxies exhibit strong variation with wavelength, but at higher average Sérsic index ( $\frac{dn}{d\lambda} = -1.10 \pm 0.23$  and  $n_0 = 1.51 \pm 0.10$ ). For the massive field galaxies we measure  $\frac{dn}{d\lambda} = -2.16 \pm 0.81$  and  $n_0 = 2.37 \pm 0.32$ . Thus indicating on average, the SMGs have light distributions closer to pure disc-like exponentials.

To further investigate the variation of morphology with wavelength in the SMG and field samples, in Figs. 10a and b, we show the Gini– $M_{20}$  relation which has been used as a crude late-stage merger indicator (Lotz et al. 2008; Liang et al. 2024; Polletta et al. 2024) in the F200W and F444W bands. We select the F444W band as this most closely traces the stellar morphology of the galaxies, whilst F200W band corresponds to the rest-frame V-band for the median redshift of the samples, at a similar wavelength to the R-band where the Gini– $M_{20}$  ‘merger’ and ‘non-merger’ boundary was calibrated by Lotz et al. (2008). At 2  $\mu\text{m}$ , (rest-frame V-band) both field and SMG samples scatter about the boundary between merger and non-merger, with  $40 \pm 5\%$  of the SMGs lying in the merger region. Although the SMGs are offset relative to the field populations with higher  $M_{20}$  and lower Gini values. At 4  $\mu\text{m}$ , (rest-frame z-band) almost all SMGs ( $92 \pm 2\%$ ) and field galaxies lie in the non-merger region of the relation, with consistent Gini and  $M_{20}$  values. Between 2  $\mu\text{m}$  and 4  $\mu\text{m}$ , the relative shift in the Gini– $M_{20}$  parameters is larger for the SMGs than for the field samples.

To understand the origin of this shift in the Gini– $M_{20}$  plane, in Fig. 10c we show the difference between the  $M_{20}$  parameter in the F444W and F200W bands. This plot highlights that the SMGs have higher  $M_{20}$  in the F200W than F444W band which indicates SMGs have less concentrated F200W morphologies whilst both the field and massive field galaxies have more similar  $M_{20}$  values between the two bands. The

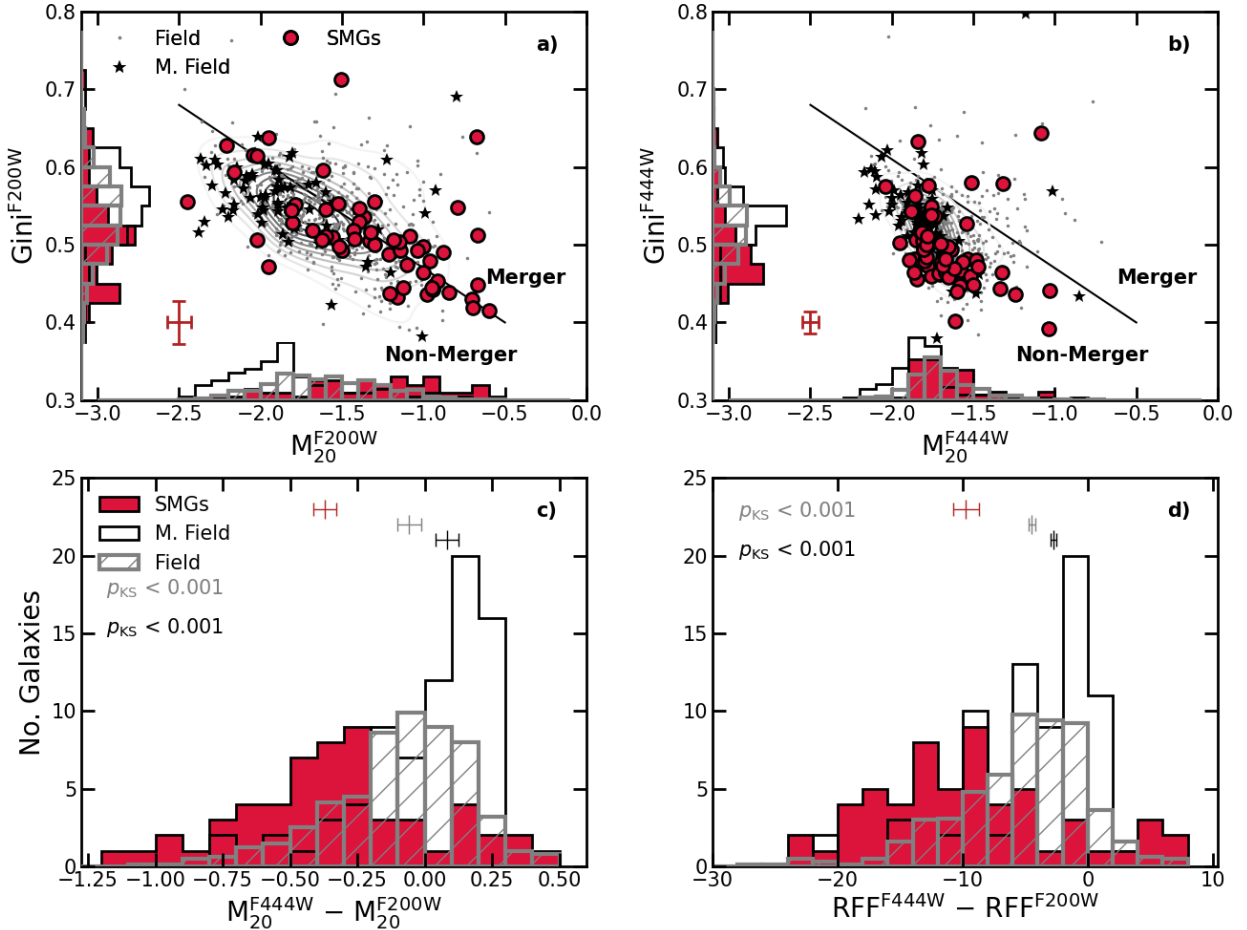


**Fig. 10.** Gini– $M_{20}$  relation for the less active field galaxies (grey dots and contours), massive field galaxies (black stars) and SMG sample (red circles), in the *a*)  $F200W$  and *b*)  $F444W$  bands as well as histograms showing the distribution of each parameter on each axis, with the low-mass field scaled down by a factor 10. The solid black line indicates the boundary line between mergers and non-mergers as defined in Lotz et al. (2008). Both SMGs and field galaxies scatter about the line in the  $F200W$  band whilst the majority lie in the non-merger region of the equivalent  $F444W$  plot. In panels *c*) and *d*) we show the distributions of  $M_{20}^{F444W} - M_{20}^{F200W}$  and  $RFF^{F444W} - RFF^{F200W}$ . For each distribution, we indicate the KS-statistic showing that the SMGs have a stronger variation in morphology with wavelength with higher RFF and  $M_{20}$  values at  $2\mu m$  than  $4\mu m$  indicating more structure in the residuals and disturbed morphologies.

significance of the difference between the field samples and SMGs is quantified by the KS-statistic value of  $p_{KS} < 0.001$ . To highlight the reduction in structured emission between the  $F200W$  and  $F444W$  bands, in Fig. 10d we show the difference between RFF in the two bands for the SMGs and field galaxies. On average the SMGs exhibit a greater difference in RFF across bands, with more significant  $F200W$  residuals, with a median value of  $RFF^{F444W} - RFF^{F200W} = -10.0 \pm 1.0$  with a 16<sup>th</sup>–84<sup>th</sup> percentile range of  $RFF^{F444W} - RFF^{F200W} = -2.0$  to  $-17.4$  whilst for the field galaxies the median is  $RFF^{F444W} - RFF^{F200W} = -4.6 \pm 0.3$  with a 16<sup>th</sup>–84<sup>th</sup> percentile range of  $RFF^{F444W} - RFF^{F200W} = -0.2$  to  $-11.6$ . The massive field galaxies have  $RFF^{F444W} - RFF^{F200W} = -3.2 \pm 0.8$  with a 16<sup>th</sup>–84<sup>th</sup> percentile range of  $RFF^{F444W} - RFF^{F200W} = -0.15$  to  $-9.5$ . This is additional evidence of the dust obscuration at shorter wavelengths in the SMGs, resulting in deviations from a simple light profile. This comparison suggests the SMGs have more complex morphologies at bluer wavelengths, which is likely to be linked to their intense star formation rates and the presence of highly structured dust in the SMGs, attenuating the shorter wavelength light.

To identify the physical mechanism driving the increase in structured emission identified in the SMGs (as quantified by

the RFF and  $M_{20}$ ) as a function of wavelength, in Fig. 11 we compare the difference in morphological parameters measured between the  $F444W$  and  $F200W$  NIRCam bands for the SMGs and field populations. In Fig. 11a we compare the dust content, as quantified by the  $A_V$  from SED fitting (Sect. 3.2), with  $M_{20}^{F444W} - M_{20}^{F200W}$ . As is shown in Fig. 3, both field samples have significantly lower  $A_V$  and less morphological variation with wavelength, with a median  $M_{20}^{F444W} - M_{20}^{F200W} = -0.06 \pm 0.01$  for the field sample and  $M_{20}^{F444W} - M_{20}^{F200W} = 0.09 \pm 0.03$  for the massive field sample. The SMGs on the other hand, with higher  $A_V$  indicate a greater disparity between the  $F200W$  and  $F444W$  light distribution with a median value of  $M_{20}^{F444W} - M_{20}^{F200W} = -0.34 \pm 0.04$ . To quantify the trend between  $A_V$  and  $M_{20}^{F444W} - M_{20}^{F200W}$  we perform an ODR fit to the running median shown in Fig. 11 of the form

$$A_V = A_{V,0} + \alpha(M_{20}^{F444W} - M_{20}^{F200W}). \quad (4)$$

We determine for the SMGs best-fit parameters of  $\alpha = -1.0 \pm 0.3$  and  $A_{V,0} = 3.1 \pm 0.1$ , indicating a strong negative correlation for the SMGs, whereby more dust obscured (higher  $A_V$ ) SMGs, have a more negative  $M_{20}^{F444W} - M_{20}^{F200W}$ , indicating less concentrated light profiles in the  $F200W$  band compared to the  $F444W$ .

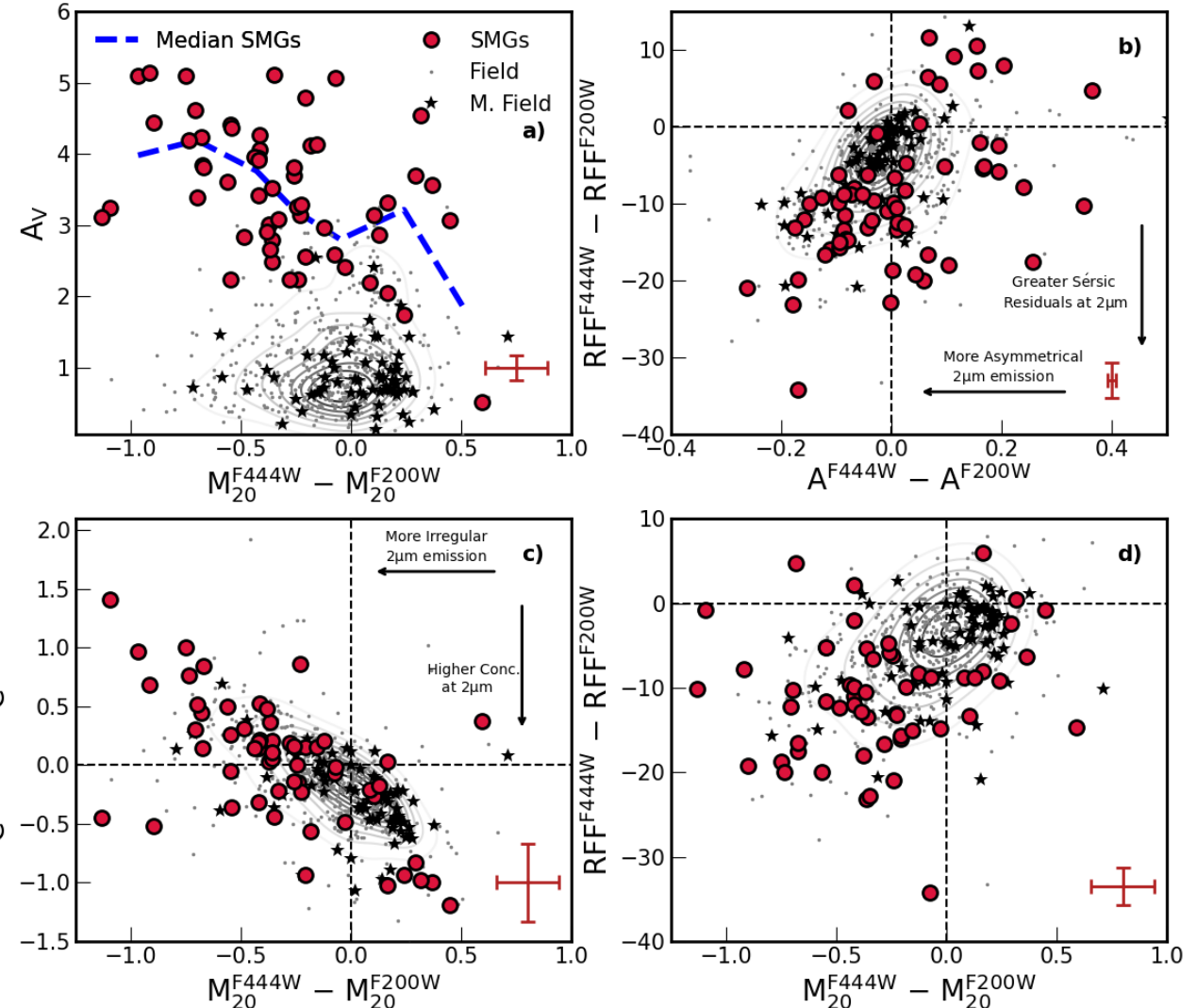


**Fig. 11.** Comparison of the  $2\mu\text{m}$  and  $4\mu\text{m}$  morphological properties of the SMGs and both field samples. We compare the difference in  $M_{20}$  parameter between the F444W and F200W bands ( $M_{20}^{\text{F444W}} - M_{20}^{\text{F200W}}$ ) with dust attenuation ( $A_V$ ) in panel *a*). In panel *b*, we further compare the difference in RFF between the F444W and F200W bands ( $\text{RFF}^{\text{F444W}} - \text{RFF}^{\text{F200W}}$ ) with the difference in Asymmetry ( $A^{\text{F444W}} - A^{\text{F200W}}$ ). Finally, we plot the difference in  $M_{20}$  between F444W and F200W ( $M_{20}^{\text{F444W}} - M_{20}^{\text{F200W}}$ ) with the difference in Concentration ( $C^{\text{F444W}} - C^{\text{F200W}}$ ) (panel *c*) and the difference in RFF (panel *d*). All four panels indicate the SMGs are much more structured than either field population, with less uniform light distributions in the F200W band compared to F444W, in contrast, the field galaxies show minimal wavelength variation.

To analyse the connection to other morphological parameters, in Figs. 11b and d we plot  $\text{RFF}^{\text{F444W}} - \text{RFF}^{\text{F200W}}$  against the difference in Asymmetry ( $A^{\text{F444W}} - A^{\text{F200W}}$ ) and  $M_{20}^{\text{F444W}} - M_{20}^{\text{F200W}}$ , whilst in Fig. 11c we compare the difference in Concentration ( $C^{\text{F444W}} - C^{\text{F200W}}$ ) with  $M_{20}^{\text{F444W}} - M_{20}^{\text{F200W}}$ . All three relations indicate that on average the SMGs in the F200W band are more asymmetric and less concentrated, with less homogeneous light distributions leading to larger residuals to a single Sérsic fit at  $2\mu\text{m}$  as compared to their  $4\mu\text{m}$  morphologies.

## 5. Discussion

### 5.1. Whether structured dust drives the differences between SMGs and field galaxies

The morphological properties of the SMGs in the NIRCam F444W band are comparable to the field galaxies, with similar sizes at a fixed mass, slightly lower Sérsic indices and higher

asymmetry (Fig. 6). The F444W filter traces the rest-frame near-infrared ( $\approx 1\mu\text{m}$ ) out to  $z \sim 3.5$ , and thus is less affected by dust obscuration and recent star formation than shorter bands in most of our sample. A greater difference between SMGs and field samples is identified at bluer wavelengths.

By investigating the variation  $M_{20}$  parameter and RFF between the NIRCam F444W band ( $\lambda_{\text{rest}} \approx 1\mu\text{m}$ ) and F200W band ( $\lambda_{\text{rest}} \approx 0.5\mu\text{m}$ ), Figs. 10 and 11 highlight that the SMGs have more structured light profiles at shorter wavelengths, which results in larger residuals to single Sérsic fits. This morphological variation with wavelength was also highlighted by Chen et al. (2016) for SMGs and Nedkova et al. (2024) for SFGs, the latter identifying that the most massive ( $M_* \gtrsim 10^{10}\text{M}_\odot$ ) disc galaxies in their sample at  $0.5 < z < 3$  have larger half-light radii in the rest-frame UV than optical, which they attribute to the significant dust attenuation in the central regions of the galaxies compared to the outskirts. A similar connection between inferred galaxy morphology and dust content was identified in the

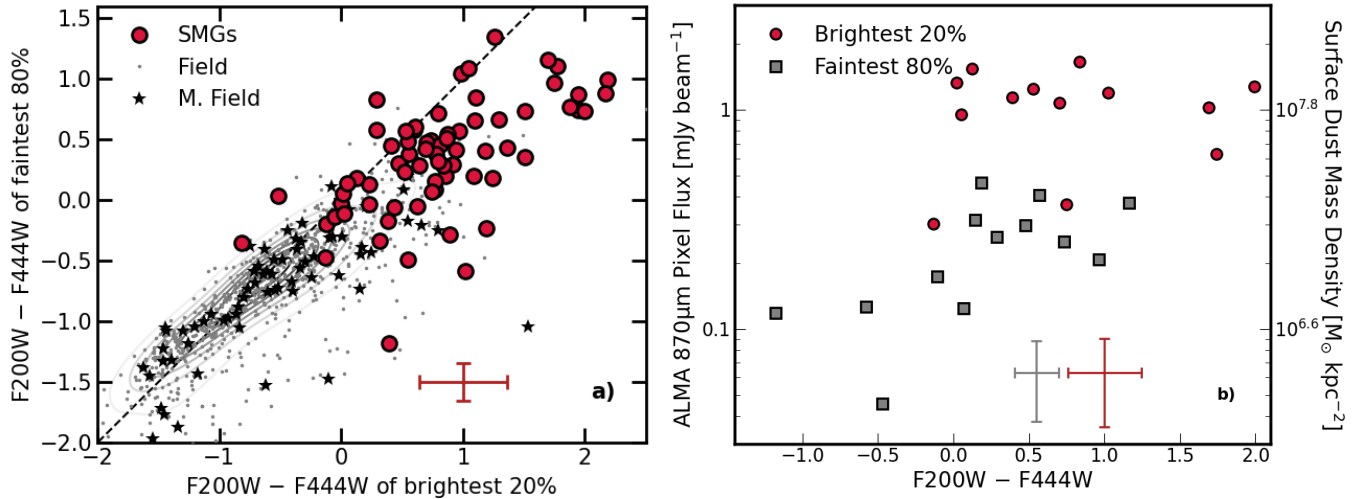


**Fig. 12.** Multi-wavelength pixel colours of SMGs and field galaxies. *a)* Average F200W – F444W colour of the faintest pixels (below 80<sup>th</sup> percentile of flux) inside 0.5'' elliptical apertures in the F444W image for the SMGs and field samples, as a function of the average colour for the top 20 percent brightest F444W pixels. Both field samples exhibit almost uniform colours between faint and bright regions, with a small offset to the equality line of  $0.12 \pm 0.03$  mag (in the sense that the brighter regions are redder). The SMGs are both generally redder in fainter regions and significantly redder ( $1.11 \pm 0.09$  mag) in their brightest regions. In panel *b*) we show the average F200W – F444W colour of the brightest 20% and faintest 80% pixels as a function of ALMA pixel brightness. On the right-hand axis we show the surface dust mass density derived using the 870  $\mu\text{m}$  flux to dust mass relation from [Dudzevičiūtė et al. \(2020\)](#) at the median redshift of the sample ( $z = 2.7$ ). The brightest regions in the near-infrared (NIRCam F444W), which have the reddest F200W – F444W colour, correspond to the brightest regions in the rest-frame far-infrared (ALMA 870  $\mu\text{m}$ ).

Illustris – The Next Generation (TNG50; [Pillepich et al. 2019](#)) simulation by [Popping et al. \(2022\)](#). They suggested that the observed  $H$ -band to 870  $\mu\text{m}$  size ratio increases towards higher redshift (hence bluer rest-frame sampling) due to dust attenuating the central regions of galaxies, resulting in larger half-light radii in the  $H$ -band. The impact of dust on size measurements has also been quantified in the First Light And Reionisation Epoch Simulations (FLARES; [Lovell et al. 2021; Vijayan et al. 2021](#)), where intrinsically massive compact galaxies appear significantly more extended when the effects of dust are taken into account ([Roper et al. 2022, 2023](#)).

To isolate the contribution of dust to the SMGs morphological evolution as a function of wavelength, we examine the F200W – F444W pixel colours. In particular, given the  $M_{20}^{\text{F444W}} - M_{20}^{\text{F200W}}$  parameter indicates the greatest morphological difference between field galaxies and SMGs, we calculate the average colour of the brightest 20 percent of pixels in the F444W image inside the 0.5'' elliptical apertures of each galaxy (Sect. 3.2). In Fig. 12a, for the SMGs and both field samples, we compare this ‘brightest 20%’ colour with the average colour of the fainter regions inside the same aperture (‘faintest 80%’ F200W – F444W). Galaxies exhibiting no strong colour gradients between bright and faint regions will have consistent brightest 20% and faintest 80% colours, lying close to the one-to-one line. The majority of the field galaxies, as well as the massive field galaxies, as is shown in Fig. 12a, fall into this regime, with the brightest regions of the field galaxies being on average  $0.12 \pm 0.03$  mag redder than the faintest.

For the SMGs, the F200W – F444W pixel colour of the fainter regions that comprise the bulk of the galaxies (faintest 80%) indicate redder colours on average, with a median colour of  $0.40 \pm 0.06$  mag compared to  $-0.74 \pm 0.02$  mag for the field galaxies and  $-0.67 \pm 0.08$  mag for the massive field galaxies. For the brightest 20% pixel colour, again the SMGs indicate significantly redder colours, with a median

value of  $0.77 \pm 0.06$  mag compared to  $-0.66 \pm 0.02$  mag for the field galaxies and  $-0.66 \pm 0.03$  mag for the massive field galaxies.

To understand whether the reddest (and brightest) regions of the SMGs are physically associated with the massive dust reservoirs, and thus 870  $\mu\text{m}$  emission, of the galaxies, we analysed high-resolution ALMA 870  $\mu\text{m}$  observations for a sub-sample of 15 SMGs with ALMA maps at  $\leq 0.2''$  FWHM resolution from [Gullberg et al. \(2019\)](#). We resampled the ALMA maps to match the 0.04 pixel scale of the JWST NIRCam F444W imaging. We then extracted the same average sub-millimetre flux density of the regions corresponding to the brightest 20% and faintest 80% F444W pixel as before for each SMG. In Fig. 12b, we correlate this pixel colour with the ALMA 870  $\mu\text{m}$  pixel brightness for the brightest 20% and faintest 80% pixels. We identify a strong correlation between F200W – F444W pixel colour and 870  $\mu\text{m}$  surface brightness, demonstrating that the redder colours that originate from the brightest regions of the SMGs are spatially correlated with the brightest regions of the 870  $\mu\text{m}$  emission, and thus high dust column density regions.

The high dust column density of the SMGs, as is shown in Fig. 12, implies that the optical to near-infrared emission of the SMGs is strongly attenuated. Consequently, physical properties estimated from the SED fitting (e.g.  $A_V$ ) may be uncertain due to more heavily obscured regions of the galaxies being undetected, a situation that will be even worse when relying solely on UV to near-infrared photometry and no energy-balance assumptions. We can derive the expected  $V$ -band extinction ( $A_V$ ) given the median dust mass ( $\log_{10}(M_d[\text{M}_\odot]) = 8.9 \pm 0.2$ ) derived from SED fitting (Sect. 3.2) and compare this to the  $A_V$  derived by magphys from fitting the optical to near-infrared SED.

As was shown by [Güver & Özel \(2009\)](#), the column density of hydrogen (in  $\text{cm}^{-2}$ ) can be approximated from the  $A_V$  (in mag) as follows:

$$N_H = 2.21 \times 10^{21} A_V. \quad (5)$$

Adopting a dust-to-gas ratio of  $\delta = 63 \pm 7$  as derived by Birkin et al. (2021), for SMGs with typical metallicity, star formation rates and stellar masses (e.g. Rémy-Ruyer et al. 2014) and assuming the F444W half-light radius provides an upper-limit on the total extent of the dust region, we obtain a lower-limit on the median  $V$ -band dust attenuation of  $A_V = 110 \pm 20$ . This is two orders of magnitude higher than that derived from the SED fitting of SMGs, with the median magphys estimated value of  $A_V = 3.40 \pm 0.16$ . For the  $A_V$  derived from magphys, which constrains the dust obscuration of the visible stars, an energy balance calculation is assumed such that far-infrared emission is broadly consistent with the absorbed stellar light of the system (Battisti et al. 2019). This assumption assumes the UV/optical and far-infrared emission are co-spatial and well mixed however, inaccuracies can arise as detectable optical emission does not encode information about the ongoing obscured star formation of the galaxy (e.g. Simpson et al. 2017; Buat et al. 2019; Haskell et al. 2023; Killi et al. 2024), with previous studies identifying a 15% uncertainty in the SFRs derived from MAGPHYS for galaxies from the EAGLE simulation (e.g. Dudzevičiūtė et al. 2020). In the derivation of  $A_V$  from the dust mass, which defines the dust obscuration of the deepest regions of the clouds, we have estimated a Compton thick HI column where the dust is uniformly distributed in a smooth disc-like component as identified in the high-resolution ALMA studies of SMGs (e.g. Hodge et al. 2016; Gullberg et al. 2019). However, numerical studies suggest that the star dust geometry plays a crucial role in determining the attenuation curve of the galaxies (e.g. Inoue 2005; Sachdeva & Nath 2022; Vijayan et al. 2024) as well as the metallicity of the ISM (e.g. Shvai et al. 2020).

## 5.2. Dust content and the interstellar medium of SMGs

As noted earlier, while the properties derived assuming energy-balance are uncertain, they would be considerably less reliable if derived solely from the UV to near-infrared photometry and no energy-balance. With such high levels of inferred dust obscuration, and intense star formation rates, the question remains as to which underlying ISM conditions give rise to these extreme physical properties in the SMGs. To infer the properties of the ISM, we compare the surface density of star formation, ( $\Sigma_{\text{SFR}}$ ), to the gas surface density ( $\Sigma_{\text{gas}}$ ); that is, the density of fuel for star formation. For the SMGs, we use the gas mass derived above, the star formation rate from MAGPHYS and the F444W half-light radius as a conservative estimate of the physical extent of the gas content. For the field sample, we use the MAGPHYS derived dust masses with a median value of  $\log_{10}(M_d[\text{M}_\odot]) = 7.7 \pm 0.1$  and  $\log_{10}(M_d[\text{M}_\odot]) = 7.6 \pm 0.1$  for the massive field, which are consistent with the dust mass inferred from converting the  $S_{870\mu\text{m}}$  limit, derived from stacks in S2CLS UDS 870  $\mu\text{m}$  map (Geach et al. 2017), to a dust mass using the  $S_{870\mu\text{m}}$  to dust mass relation defined in Dudzevičiūtė et al. (2020). Adopting the metallicity-dependent dust-to-gas ratio from Tacconi et al. (2018) for massive SFGs and following the mass metallicity relation defined in Genzel et al. (2015), we derive a median dust-to-gas ratio of  $\delta = 163 \pm 32$  which equates to a median gas mass of  $\log_{10}(M_g[\text{M}_\odot]) = 9.8 \pm 0.1$  for the field galaxies. Following the same procedure but for the massive field galaxies, we derive a median gas mass of  $\log_{10}(M_g[\text{M}_\odot]) = 9.9 \pm 0.1$  for the massive field sample.

Combining this gas mass estimate for the field samples with the MAGPHYS derived star formation rates and F444W half-light radius, in Fig. 13 we show the relation between  $\Sigma_{\text{SFR}}$  and  $\Sigma_{\text{gas}}$  for both the field populations and SMGs. Given the higher star for-

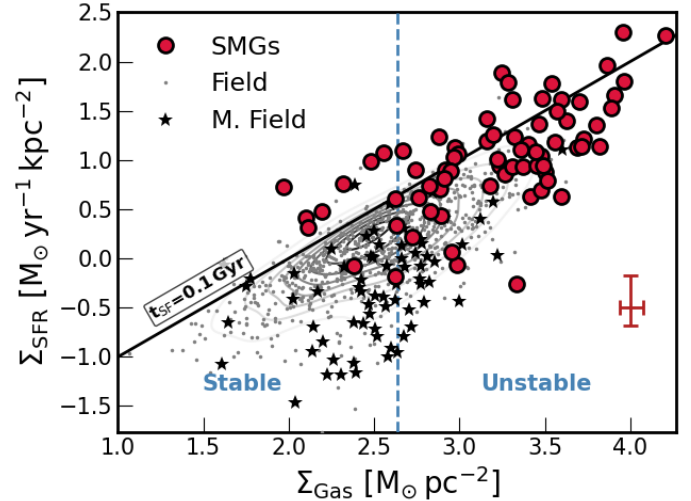


**Fig. 13.** Relation between star formation rate surface density and gas surface density for the field sample (grey points and contour) and massive field sample (black stars) and SMGs (red circles). We indicate a constant star formation timescale of 0.1 Gyr with the black line. Adopting the typical rotation velocity and velocity dispersion from Birkin et al. (2024) derived for a sample of AS2UDS SMGs, we define the boundary between stable ( $Q > 1$ ) and unstable ( $Q < 1$ ) gas discs. The majority of the SMGs indicate unstable gas discs with a median Toomre  $Q$  parameter of  $Q = 0.47 \pm 0.06$  while most of the field samples are stable or marginally stable.

mation rates and dust masses of the SMGs (Fig. 3) and their comparable sizes in the F444W band to the field galaxies (Fig. 6), the SMGs have considerably higher star formation rate surface density and gas surface density. However, both the lower mass field galaxies and SMGs have comparable timescales for star formation, lying close to the 0.1 Gyr star formation timescale. The massive field sample has lower  $\Sigma_{\text{SFR}}$ , due to their lower specific star formation rates (Fig. 6).

By estimating the Toomre  $Q$  parameter (Toomre 1964) we can place constraints on the ISM properties of the galaxies, in particular on the stability of the gas disc. The Toomre  $Q$  is defined as

$$Q = \frac{\sigma \kappa}{\pi G \Sigma_{\text{gas}}}, \quad (6)$$

where  $\sigma$  is the radial velocity dispersion,  $\kappa$  is the epicyclic frequency, for which we adopt  $\kappa = \sqrt{V}R$  appropriate for a galaxy with a flat rotation curve, and  $\Sigma_{\text{gas}}$  is the gas surface density. For the rotation velocity and velocity dispersion, we adopt the median values from Birkin et al. (2024), for a sample 31 SMGs in the AS2UDS survey, with comparable median redshift and stellar mass to our sample ( $z \sim 1.3\text{--}2.6$ ,  $\log_{10}(M_*[\text{M}_\odot]) = 11.11 \pm 0.06$ ). Birkin et al. (2024) derive a median rotation velocity and velocity dispersion of  $V_{\text{circ}} = 230 \pm 20 \text{ km s}^{-1}$  and  $\sigma = 87 \pm 6 \text{ km s}^{-1}$ .

Adopting the F444W half-light radius as an estimate of the extent of the gas disc, we can derive the gas-surface density required for a quasi-stable gas disc, identifying a threshold value of  $\log_{10}(\Sigma_{\text{gas}}) = 2.64 \pm 0.05 \text{ M}_\odot \text{ pc}^{-2}$ . This implies the gas disc is unstable to collapse ( $Q < 1$ ) for gas-surface densities higher than this value. We estimate that the majority of the SMGs lie in this region of ‘instability’ with a median Toomre  $Q$  parameter of  $Q = 0.47 \pm 0.06$ , while the bulk of the field samples are stable ( $Q > 1$ ) or marginally stable ( $Q \approx 1$ ).

To test the sensitivity of these conclusions on our assumptions, we note that given the F444W half-light radius provides a lower limit on the extent of the gas disc. Thus to generate a quasi-stable ISM in the SMGs, we require a larger rotation velocity or velocity dispersion. If the gas disc is required to be quasi-stable i.e.  $Q \geq 1$ , we derive a lower limit on the radial velocity dispersion needed. Adopting the rotation velocity from Birkin et al. (2024), we derive a median velocity dispersion for stability of  $\sigma_{\text{stable}} \geq 200 \pm 30 \text{ km s}^{-1}$  which is significantly larger than that derived for ionised gas in previous studies of high redshift SMGs or U/LIRGS (e.g. Hogan et al. 2021; Birkin et al. 2024; Amvrosiadis et al. 2024), suggesting that the gaseous discs of the SMGs in our sample are very likely unstable to gravitational collapse.

### 5.3. Implications for the nature of SMGs

The SMG and field samples employed in our analysis share several characteristics. By construction, they have similar number densities as a function of redshift with the larger field sample matched in specific star formation rate over  $z \approx 1-5$  and the massive field sample matched in stellar mass over  $z \approx 1-3$ . Furthermore, we have demonstrated they have similar rates of mergers and signatures of disturbance, as well as comparable rest-frame near-infrared axis ratios and (mass normalised) stellar continuum (F444W) sizes. This suggests that the major structural components in both populations comprise (randomly orientated) discs that broadly follow the size-mass relation for disc galaxies at  $z \sim 2-3$ . The similarity in the merger fractions for the SMGs and field is consistent with the theoretical investigation of SMGs in the EAGLE simulation by McAlpine et al. (2019), who concluded that there was no difference in merger statistics of SMGs and the general population in the simulations, instead, most massive galaxies at these redshifts were undergoing minor or major mergers.

However, there are several distinctions between the SMGs and the less active field samples. The dust-mass-selected SMGs have much higher  $A_V$  and asymmetry, and they show stronger variations in their morphologies at bluer wavelengths, indicating the presence of structured and centrally concentrated dust. Moreover, both field samples have an average Sérsic index of  $n \gtrsim 2$ , indicating the potential presence of a bulge component in these systems. While the SMGs have consistently lower Sérsic index, with a median of  $n \sim 1.1$ , indicating they are nearly pure exponential discs or that any bulge component if present is invisible at rest-frame  $\sim 1 \mu\text{m}$ . Both of these interpretations suggest that any bulge component in the SMGs is of low mass compared to the disc or is likely to be young and so only recently formed.

We also infer more than an order of magnitude higher molecular gas surface densities for the SMGs than the field. These differences suggest that one possible cause for a distinction between SMGs and less active galaxies arises from the less developed bulge components present in the SMGs (see McAlpine et al. 2019). Consequently, their gas discs are both more massive and also more sensitive to developing low-order disc instabilities, including  $m=1$  bars (e.g. Marinova & Jogee 2007; Pettitt & Wadsley 2018). These instabilities can either be triggered by external perturbations from major or minor mergers or tidal interactions, or from secular instabilities in the dense gas discs. These structures, as predicted by theoretical models (e.g. Fragkoudi et al. 2021; Bland-Hawthorn et al. 2023) and identified in recent studies of individual high-redshift SMGs (e.g. Hodge et al. 2019; Smail et al. 2023; Amvrosiadis et al. 2024) serve to funnel gas from the dense gas disc into the central

regions of the galaxies, driving a central starburst that creates both the compact sub-millimetre emission we see and the corresponding highly obscured central regions of these systems.

To assess the possible subsequent structured evolution of the SMGs, we followed the prescription of Brennan et al. (2015) that relates B/T to the Sérsic index. Adopting the F444W/870  $\mu\text{m}$  =  $2.7 \pm 0.4$  as the ratio of the disc to bulge size, the SMGs at  $z = 2.7 \pm 0.2$  with a  $n_{\text{F444W}} = 1.1 \pm 0.1$  have a bulge-to-total ratio of  $B/T = 0.16 \pm 0.12$ . If the SMGs converted their gas mass (which we assume to be equivalent to 50% of their stellar mass following Birkin et al. 2021) to a bulge component, it would result in a  $B/T = 0.49 \pm 0.18$  which following Brennan et al. (2015) gives a Sérsic index of  $n = 2.2 \pm 0.8$ . This is consistent with the Sérsic index measure for the gas-poor bulge-strong massive field sample, which suggests that the field galaxies may have already experienced their SMG phase at an earlier epoch and the SMGs may evolve to a gas-poor bulge-strong massive but less active population population within the next  $\approx 0.1$  Gyr.

## 6. Conclusions

We present a multi-wavelength morphological analysis of a complete sample of ALMA-identified sub-millimetre-selected galaxies from the AS2UDS and AS2COSMOS surveys (Stach et al. 2019; Simpson et al. 2020) with  $>4.5\sigma$  ALMA 870  $\mu\text{m}$  detections and positions. Utilising public JWST/NIRCam and MIRI imaging from the PRIMER survey, we have built a sample of 80 SMGs, determining their multi-wavelength properties through an SED and morphological analysis. We have further defined two matched samples of less active and more typical  $K$ -band selected star-forming field galaxies in the UDS field and analysed the differences between the populations. Our main conclusions are:

- From visually inspecting the F277W/F356W/F444W colour images and F444W GALFIT residual maps of the SMGs, we identify  $20 \pm 5\%$  as candidate major mergers, a further  $40 \pm 10\%$  as potential minor mergers, and the remaining 40% as isolated undisturbed systems. We find no dependence of the visual classification on far-infrared luminosity, with similar statistics identified in the field samples, suggesting that the majority of SMGs are not ongoing major mergers, although mergers (major or minor) and disturbed appearances are common in both the SMGs and the less active field population at these redshifts.
- The SMG and field populations are more distinct in their detailed morphologies in terms of Sérsic index ( $n$ ) and Asymmetry ( $A$ ) in the F444W band, with the SMGs having lower Sérsic indices and higher Asymmetry ( $n_{\text{F444W}} = 1.1 \pm 0.1$ ,  $A_{\text{F444W}} = 0.13 \pm 0.02$ ) compared to both the less massive field galaxies ( $n_{\text{F444W}} = 1.9 \pm 0.1$ ,  $A_{\text{F444W}} = 0.08 \pm 0.01$ ) or the more and massive field galaxies ( $n_{\text{F444W}} = 2.8 \pm 0.2$ ,  $A_{\text{F444W}} = 0.07 \pm 0.02$ ).
- A similar disparity between the SMGs and typical SFGs is seen in the variation of their morphologies as a function of wavelength. The size of the SMGs declines more rapidly at longer wavelengths than both field populations ( $\delta(R_h/R_{1\mu\text{m}})/\delta\lambda = -0.60 \pm 0.09$  versus  $\delta(R_h/R_{1\mu\text{m}})/\delta\lambda = -0.15 \pm 0.07$  for the low-mass field sample or  $\delta(R_h/R_{1\mu\text{m}})/\delta\lambda = -0.04 \pm 0.09$  for the massive field sample), with the SMGs exhibiting lower Sérsic indices at all wavelengths.
- We have further determined that the brightest and reddest regions of the SMGs in the NIRCam imaging correspond to

the highest surface brightness emission at  $870\text{ }\mu\text{m}$  seen by ALMA, indicating a strong connection between the colour and the local dust columns in the galaxies on  $\simeq$  kiloparsec scales.

- To understand the physical origin of the difference in morphologies between the SMGs and the field galaxies, we have assumed a representative gas-to-dust ratio to define the relation between the star formation rate surface density and the gas surface density, suggesting that the SMGs have significantly higher gas surface densities than field galaxies. The SMGs on average fall in the unstable ( $Q < 1$ ) regime with a median Toomre  $Q$  parameter of  $Q = 0.47 \pm 0.06$ , while the bulk of the field populations are stable or marginally stable ( $Q \gtrsim 1$ ).

Our analysis indicates that SMGs and typical SFGs appear morphologically distinct in the rest-frame optical due to the higher dust content of the SMGs, which preferentially influences the central regions of the galaxies. While at longer wavelengths, sampling the rest-frame near-infrared, the SMGs and less active field galaxies show more similar mass-normalised sizes, although the SMGs exhibit lower Sérsic parameters, suggesting that they have weaker bulge components. Both the SMGs and field control samples have comparable rates of mergers and undisturbed galaxies, suggesting that mergers are not a unique driver of the activity in SMGs (as is indicated by previous theoretical studies, [McAlpine et al. 2019](#)). Instead, we suggest that the higher gas surface densities and weaker bulge components (which may be linked through previous evolution), coupled with the perturbations caused by either major or minor mergers, as well as secular processes, lead to correspondingly more intense star formation activity in the SMGs, compared to the field. Thus, the defining characteristic of SMGs may be their massive and gas-rich nature, coupled with relatively underdeveloped bulge components and correspondingly low black hole masses (see [McAlpine et al. 2019](#)).

## Data availability

Table A.2 is available at the CDS via anonymous ftp to [cdsarc.cds.unistra.fr](http://cdsarc.cds.unistra.fr) (130.79.128.5) or via <https://cdsarc.cds.unistra.fr/viz-bin/cat/J/A+A/691/A299>

A full version of Appendix B is available at <https://zenodo.org/records/13805467>

**Acknowledgements.** We would like to thank the PRIMER team for designing and executing the observations upon which this work is based. The observations analysed in this work are made with the NASA/ESA/CSA *James Webb* Space Telescope (DOI: [10.17909/z7p0-8481](https://doi.org/10.17909/z7p0-8481)). Certain aspects of the analysis in this paper were undertaken on SCUBA-2 data taken as part of Program ID MJLSC02. SG acknowledges financial support from the Villum Young Investigator grants 37440 and 13160 and the Cosmic Dawn Center (DAWN), funded by the Danish National Research Foundation (DNRF) under grant No. 140. IRS and AMS acknowledge STFC grant ST/X001075/1. BG acknowledges support from the Carlsberg Foundation Research Grant CF20-0644 ‘Physical pRoperties of the InterStellar Medium in Luminous Infrared Galaxies at High redshift: PRISM- LIGHT’. TRG is grateful for support from the Carlsberg Foundation via grant No. CF20-0534. YM acknowledges support of JSPS KAKENHI Grant Numbers JP17KK0098, JP22H01273 and JP23K22544. C.-C.C. acknowledges support from the National Science and Technology Council of Taiwan (NSTC 111-2112M-001-045MY3), as well as Academia Sinica through the Career Development Award (AS-CDA-112-M02). This work made use of the following open-source software: Astropy ([Astropy Collaboration 2013, 2018](#)), Photutils ([Bradley et al. 2022](#)), Source Extractor ([Bertin & Arnouts 1996](#)), SEP ([Barbary et al. 2016](#)), Eazy-py ([Brammer & Matharu 2021](#)), GriZLi ([Brammer et al. 2022](#)), GalfitM ([Häubler et al. 2013](#)), Statmorph ([Rodriguez-Gomez et al. 2019](#)), Topcat ([Taylor 2005](#)). Cloud-based data processing and file storage for this work is provided by the AWS Cloud Credits for Research program. The data products presented

herein were retrieved from the Dawn JWST Archive (DJA). DJA is an initiative of the Cosmic Dawn Center, which is funded by the Danish National Research Foundation under grant No. 140

## References

- Abraham, R. G., van den Bergh, S., & Nair, P. 2003, [ApJ, 588, 218](#)
- Aguirre, P., Baker, A. J., Menanteau, F., Lutz, D., & Tacconi, L. J. 2013, [ApJ, 768, 164](#)
- Alaghband-Zadeh, S., Chapman, S. C., Swinbank, A. M., et al. 2012, [MNRAS, 424, 2232](#)
- Alberts, S., Wilson, G. W., Lu, Y., et al. 2013, [MNRAS, 431, 194](#)
- Amvrosiadis, A., Eales, S. A., Negrello, M., et al. 2018, [MNRAS, 475, 4939](#)
- Amvrosiadis, A., Wardlow, J. L., Birk, J. E., et al. 2023, ArXiv e-prints [[arXiv:2312.08959](#)]
- Amvrosiadis, A., Lange, S., Nightingale, J., et al. 2024, ArXiv e-prints [[arXiv:2404.01918](#)]
- An, F. X., Stach, S. M., Smail, I., et al. 2018, [ApJ, 862, 101](#)
- Aniano, G., Draine, B. T., Hunt, L. K., et al. 2020, [ApJ, 889, 150](#)
- Astropy Collaboration (Robitaille, T. P., et al.) 2013, [A&A, 558, A33](#)
- Astropy Collaboration (Price-Whelan, A. M., et al.) 2018, [AJ, 156, 123](#)
- Barbary, K., Boone, K., McCully, C., et al. 2016, <https://doi.org/10.5281/zenodo.159035>
- Battisti, A. J., da Cunha, E., Grasha, K., et al. 2019, [ApJ, 882, 61](#)
- Baugh, C. M., Lacey, C. G., Frenk, C. S., et al. 2005, [MNRAS, 356, 1191](#)
- Bendo, G. J., Urquhart, S. A., Serjeant, S., et al. 2023, [MNRAS, 522, 2995](#)
- Bertin, E., & Arnouts, S. 1996, [A&AS, 117, 393](#)
- Birk, J. E., Weiss, A., Wardlow, J. L., et al. 2021, [MNRAS, 501, 3926](#)
- Birk, J. E., Puglisi, A., Swinbank, A. M., et al. 2024, [MNRAS, 531, 61](#)
- Bland-Hawthorn, J., Tepper-Garcia, T., Agertz, O., & Freeman, K. 2023, [ApJ, 947, 80](#)
- Bouwens, R., González-López, J., Aravena, M., et al. 2020, [ApJ, 902, 112](#)
- Bradley, L., Sipőcz, B., Robitaille, T., et al. 2022, <https://doi.org/10.5281/zenodo.6825092>
- Brammer, G., & Matharu, J. 2021, <https://doi.org/10.5281/zenodo.5012699>
- Brammer, G., Strait, V., Matharu, J., & Momcheva, I. 2022, <https://doi.org/10.5281/zenodo.6672538>
- Brennan, R., Pandya, V., Somerville, R. S., et al. 2015, [MNRAS, 451, 2933](#)
- Buat, V., Ciesla, L., Boquien, M., Małek, K., & Burgarella, D. 2019, [A&A, 632, A79](#)
- Calistro Rivera, G., Hodge, J. A., Smail, I., et al. 2018, [ApJ, 863, 56](#)
- Casey, C. M., Chen, C.-C., Cowie, L. L., et al. 2013, [MNRAS, 436, 1919](#)
- Chabrier, G. 2003, [PASP, 115, 763](#)
- Chapman, S. C., Smail, I., Ivison, R. J., & Blain, A. W. 2002, [MNRAS, 335, L17](#)
- Chapman, S. C., Windhorst, R., Odewahn, S., Yan, H., & Conselice, C. 2003, [ApJ, 599, 92](#)
- Chapman, S. C., Smail, I., Windhorst, R., Muxlow, T., & Ivison, R. J. 2004, [ApJ, 611, 73](#)
- Chen, C.-C., Smail, I., Swinbank, A. M., et al. 2015, [ApJ, 799, 194](#)
- Chen, C.-C., Smail, I., Swinbank, A. M., et al. 2016, [ApJ, 831, 91](#)
- Chen, C.-C., Hodge, J. A., Smail, I., et al. 2017, [ApJ, 846, 108](#)
- Chen, C.-C., Harrison, C. M., Smail, I., et al. 2020, [A&A, 635, A119](#)
- Chen, C.-C., Gao, Z.-K., Hsu, Q.-N., et al. 2022, [ApJ, 939, L7](#)
- Cheng, C., Huang, J.-S., Smail, I., et al. 2023, [ApJ, 942, L19](#)
- Cochrane, R. K., Best, P. N., Smail, I., et al. 2021, [MNRAS, 503, 2622](#)
- Cochrane, R. K., Anglés-Alcázar, D., Cullen, F., & Hayward, C. C. 2024, [ApJ, 961, 37](#)
- Conselice, C. J., Chapman, S. C., & Windhorst, R. A. 2003, [ApJ, 596, L5](#)
- Cowie, L. L., González-López, J., Barger, A. J., et al. 2018, [ApJ, 865, 106](#)
- Cunha, E., Walter, F., Smail, I. R., et al. 2015, [ApJ, 806, 110](#)
- Downes, A. J. B., Peacock, J. A., Savage, A., & Carrie, D. R. 1986, [MNRAS, 218, 31](#)
- Draine, B. T., Dale, D. A., Bendo, G., et al. 2007, [ApJ, 663, 866](#)
- Drew, P. M., Casey, C. M., Cooray, A., & Whitaker, K. E. 2020, [ApJ, 892, 104](#)
- Dudzevičiūtė, U., Smail, I., Swinbank, A. M., et al. 2020, [MNRAS, 494, 3828](#)
- Dunlop, J. S., McLure, R. J., Biggs, A. D., et al. 2017, [MNRAS, 466, 861](#)
- Dunlop, J. S., Abraham, R. G., Ashby, M. L. N., et al. 2021, PRIMER: Public Release IMaging for Extragalactic Research, JWST Proposal. Cycle 1, ID: #1837
- Engel, H., Tacconi, L. J., Davies, R. I., et al. 2010, [ApJ, 724, 233](#)
- Faisst, A. L., Brinch, M., Casey, C. M., et al. 2024, ArXiv e-prints [[arXiv:2405.09619](#)]
- Farrah, D., Rowan-Robinson, M., Oliver, S., et al. 2001, [MNRAS, 326, 1333](#)
- Fazio, G. G., Hora, J. L., Allen, L. E., et al. 2004, [ApJS, 154, 10](#)
- Fragkoudi, F., Grand, R. J. J., Pakmor, R., et al. 2021, [A&A, 650, L16](#)
- Fruchter, A. S., & Hook, R. N. 2002, [PASP, 114, 144](#)

- Fujimoto, S., Ouchi, M., Shibuya, T., & Nagai, H. 2017, *ApJ*, 850, 83  
 Gaia Collaboration, A., Brown, A. G. A., et al. 2021, *A&A*, 649, A1  
 Gardner, J. P., Mather, J. C., Abbott, R., et al. 2023, *PASP*, 135, 068001  
 Geach, J. E., Dunlop, J. S., Halpern, M., et al. 2017, *MNRAS*, 465, 1789  
 Genzel, R., Tacconi, L. J., Lutz, D., et al. 2015, *ApJ*, 800, 20  
 Gillman, S., Gullberg, B., Brammer, G., et al. 2023, *A&A*, 676, A26  
 Gómez-Guijarro, C., Toft, S., Karim, A., et al. 2018, *ApJ*, 856, 121  
 Greve, T. R., Bertoldi, F., Smail, I., et al. 2005, *MNRAS*, 359, 1165  
 Grogin, N. A., Kocevski, D. D., Faber, S. M., et al. 2011, *ApJS*, 197, 35  
 Gullberg, B., Smail, I., Swinbank, A. M., et al. 2019, *MNRAS*, 490, 4956  
 Guo, Y., Jogee, S., Finkelstein, S. L., et al. 2023, *ApJ*, 945, L10  
 Güver, T., & Özel, F. 2009, *MNRAS*, 400, 2050  
 Haskell, P., Smith, D. J. B., Cochrane, R. K., Hayward, C. C., & Anglés-Alcázar, D. 2023, *MNRAS*, 525, 1535  
 Häußler, B., Bamford, S. P., Vika, M., et al. 2013, *MNRAS*, 430, 330  
 Hayward, C. C., Narayanan, D., Kereš, D., et al. 2013, *MNRAS*, 428, 2529  
 Hodge, J. A., & da Cunha, E. 2020, *R. Soc. Open Sci.*, 7, 200556  
 Hodge, J. A., Carilli, C. L., Walter, F., et al. 2012, *ApJ*, 760, 11  
 Hodge, J. A., Karim, A., Smail, I., et al. 2013, *ApJ*, 768, 91  
 Hodge, J. A., Swinbank, A. M., Simpson, J. M., et al. 2016, *ApJ*, 833, 103  
 Hodge, J. A., Smail, I., Walter, F., et al. 2019, *ApJ*, 876, 130  
 Hogan, L., Rigopoulou, D., Magdis, G. E., et al. 2021, *MNRAS*, 503, 5329  
 Hopkins, P. F., Younger, J. D., Hayward, C. C., Narayanan, D., & Hernquist, L. 2010, *MNRAS*, 402, 1693  
 Hoyos, C., den Brok, M., Verdoes Kleijn, G., et al. 2011, *MNRAS*, 411, 2439  
 Hoyos, C., Aragón-Salamanca, A., Gray, M. E., et al. 2012, *MNRAS*, 419, 2703  
 Hwang, Y.-H., Wang, W.-H., Chang, Y.-Y., et al. 2021, *ApJ*, 913, 6  
 Ikarashi, S., Ivison, R. J., Caputi, K. I., et al. 2015, *ApJ*, 810, 133  
 Ikarashi, S., Ivison, R. J., Cowley, W. I., & Kohno, K. 2022, *A&A*, 659, A154  
 Inoue, A. K. 2005, *MNRAS*, 359, 171  
 Ivison, R. J., Greve, T. R., Smail, I., et al. 2002, *MNRAS*, 337, 1  
 Ivison, R. J., Greve, T. R., Serjeant, S., et al. 2004, *ApJS*, 154, 124  
 Ivison, R. J., Richard, J., Biggs, A. D., et al. 2020, *MNRAS*, 495, L1  
 Kamieneski, P. S., Frye, B. L., Pascale, M., et al. 2023, *ApJ*, 955, 91  
 Kartaltepe, J. S., Sanders, D. B., Le Floc'h, E., et al. 2010, *ApJ*, 721, 98  
 Killi, M., Ginolfi, M., Popping, G., et al. 2024, ArXiv e-prints [arXiv:2402.07982]  
 Kirkpatrick, A., Pope, A., Charmandaris, V., et al. 2013, *ApJ*, 763, 123  
 Kirkpatrick, A., Alberts, S., Pope, A., et al. 2017, *ApJ*, 849, 111  
 Kokorev, V., Brammer, G., Fujimoto, S., et al. 2022, *ApJS*, 263, 38  
 Kokorev, V., Jin, S., Gómez-Guijarro, C., et al. 2023, *A&A*, 677, A172  
 Kron, R. G. 1980, *ApJS*, 43, 305  
 Lang, P., Schinnerer, E., Smail, I., et al. 2019, *ApJ*, 879, 54  
 Lawrence, A., Warren, S. J., Almaini, O., et al. 2007, *MNRAS*, 379, 1599  
 Lelli, F., Di Teodoro, E. M., Fraternali, F., et al. 2021, *Science*, 371, 713  
 Liang, P., Dai, Y. S., Huang, J. S., Cheng, C., & Yaru, S. 2024, ArXiv e-prints [arXiv:2405.06984]  
 Ling, C., & Yan, H. 2022, *ApJ*, 929, 40  
 Liu, Z., Silverman, J. D., Daddi, E., et al. 2023, ArXiv e-prints [arXiv:2311.14809]  
 Long, A. S., Casey, C. M., del P. Lagos, C., et al. 2023, *ApJ*, 953, 11  
 Lotz, J. M., Primack, J., & Madau, P. 2004, *AJ*, 128, 163  
 Lotz, J. M., Davis, M., Faber, S. M., et al. 2008, *ApJ*, 672, 177  
 Lovell, C. C., Vijayan, A. P., Thomas, P. A., et al. 2021, *MNRAS*, 500, 2127  
 Lovell, C. C., Geach, J. E., Davé, R., et al. 2022, *MNRAS*, 515, 3644  
 Lower, S., Narayanan, D., Li, Q., & Davé, R. 2023, *ApJ*, 950, 94  
 Magnelli, B., Lutz, D., Santini, P., et al. 2012, *A&A*, 539, A155  
 Marinova, I., & Jogee, S. 2007, *ApJ*, 659, 1176  
 Martorano, M., van der Wel, A., Baes, M., et al. 2024, ArXiv e-prints [arXiv:2406.17756]  
 McAlpine, S., Smail, I., Bower, R. G., et al. 2019, *MNRAS*, 488, 2440  
 McKinney, J., Casey, C. M., Long, A. S., et al. 2024, ArXiv e-prints [arXiv:2408.08346]  
 McLure, R. J., Pentericci, L., Cimatti, A., et al. 2018, *MNRAS*, 479, 25  
 Miettinen, O., Delvecchio, I., Smolčić, V., et al. 2017a, *A&A*, 602, L9  
 Miettinen, O., Delvecchio, I., Smolčić, V., et al. 2017b, *A&A*, 606, A17  
 Mitsuhashi, I., Matsuda, Y., Smail, I., et al. 2021, *ApJ*, 907, 122  
 Nedkova, K. V., Rafelski, M., Teplitz, H. I., et al. 2024, ArXiv e-prints [arXiv:2405.10908]  
 Pearson, J., Serjeant, S., Wang, W.-H., et al. 2024, *MNRAS*, 527, 12044  
 Peng, C. Y., Ho, L. C., Impey, C. D., & Rix, H.-W. 2010, *AJ*, 139, 2097  
 Perrin, M. D., Sivaramakrishnan, A., Lajoie, C.-P., et al. 2014, *SPIE Conf. Ser.*, 9143, 91433X  
 Pettitt, A. R., & Wadsley, J. W. 2018, *MNRAS*, 474, 5645  
 Pillepich, A., Nelson, D., Springel, V., et al. 2019, *MNRAS*, 490, 3196  
 Polletta, M., Frye, B. L., Garuda, N., et al. 2024, *A&A*, 690, A285  
 Popping, G., Pillepich, A., Calistro Rivera, G., et al. 2022, *MNRAS*, 510, 3321  
 Price, S. H., Suess, K. A., Williams, C. C., et al. 2023, ArXiv e-prints [arXiv:2310.02500]  
 Rémy-Ruyer, A., Madden, S. C., Galliano, F., et al. 2014, *A&A*, 563, A31  
 Ren, J., Liu, F. S., Li, N., et al. 2024, ArXiv e-prints [arXiv:2404.16686]  
 Rizzo, F., Vegetti, S., Fraternali, F., Stacey, H. R., & Powell, D. 2021, *MNRAS*, 507, 3952  
 Rodriguez-Gomez, V., Snyder, G. F., Lotz, J. M., et al. 2019, *MNRAS*, 483, 4140  
 Roper, W. J., Lovell, C. C., Vijayan, A. P., et al. 2022, *MNRAS*, 514, 1921  
 Roper, W. J., Lovell, C. C., Vijayan, A. P., et al. 2023, *MNRAS*, 526, 6128  
 Rowlands, K., Dunne, L., Dye, S., et al. 2014, *MNRAS*, 441, 1017  
 Rujopakarn, W., Williams, C. C., Daddi, E., et al. 2023, *ApJ*, 948, L8  
 Sachdeva, S., & Nath, B. B. 2022, *MNRAS*, 513, L63  
 Sanders, D. B., Soifer, B. T., Elias, J. H., et al. 1988, *ApJ*, 325, 74  
 Scoville, N., Aussel, H., Brusa, M., et al. 2007, *ApJS*, 172, 1  
 Shivaei, I., Reddy, N., Rieke, G., et al. 2020, *ApJ*, 899, 117  
 Shivaei, I., Alberts, S., Florian, M., et al. 2024, *A&A*, 690, A89  
 Simpson, J. M., Swinbank, A. M., Smail, I., et al. 2014, *ApJ*, 788, 125  
 Simpson, J. M., Smail, I., Swinbank, A. M., et al. 2015, *ApJ*, 807, 128  
 Simpson, J. M., Smail, I., Swinbank, A. M., et al. 2017, *ApJ*, 839, 58  
 Simpson, J. M., Smail, I., Swinbank, A. M., et al. 2019, *ApJ*, 880, 43  
 Simpson, J. M., Smail, I., Dudzevičiūtė, U., et al. 2020, *MNRAS*, 495, 3409  
 Smail, I., Ivison, R. J., Blain, A. W., & Kneib, J. P. 1998, *ApJ*, 507, L21  
 Smail, I., Dudzevičiūtė, U., Stach, S. M., et al. 2021, *MNRAS*, 502, 3426  
 Smail, I., Dudzevičiūtė, U., Gurwell, M., et al. 2023, *ApJ*, 958, 36  
 Snyder, G. F., Torrey, P., Lotz, J. M., et al. 2015, *MNRAS*, 454, 1886  
 Stach, S. M., Dudzevičiūtė, U., Smail, I., et al. 2019, *MNRAS*, 487, 4648  
 Suess, K. A., Bezanson, R., Nelson, E. J., et al. 2022, *ApJ*, 937, L33  
 Sun, F., Helton, J. M., Egami, E., et al. 2024, *ApJ*, 961, 69  
 Swinbank, A. M., Lacey, C. G., Smail, I., et al. 2008, *MNRAS*, 391, 420  
 Swinbank, A. M., Smail, I., Chapman, S. C., et al. 2010, *MNRAS*, 405, 234  
 Swinbank, A. M., Simpson, J. M., Smail, I., et al. 2014, *MNRAS*, 438, 1267  
 Tacconi, L. J., Genzel, R., Smail, I., et al. 2008, *ApJ*, 680, 246  
 Tacconi, L. J., Genzel, R., Saintonge, A., et al. 2018, *ApJ*, 853, 179  
 Taylor, M. B. 2005, *ASP Conf. Ser.*, 347, 29  
 Toomre, A. 1964, *ApJ*, 139, 1217  
 Vijayan, A. P., Lovell, C. C., Wilkins, S. M., et al. 2021, *MNRAS*, 501, 3289  
 Vijayan, A. P., Thomas, P. A., Lovell, C. C., et al. 2024, *MNRAS*, 527, 7337  
 Ward, E., de la Vega, A., Mobasher, B., et al. 2024, *ApJ*, 962, 176  
 Wardlow, J. L., Smail, I., Coppin, K. E. K., et al. 2011, *MNRAS*, 415, 1479  
 Wel, A., Bell, E. F., Häussler, B., et al. 2012, *ApJS*, 203, 24  
 Wel, A., Martorano, M., Häußler, B., et al. 2024, *ApJ*, 960, 53  
 Wu, Y., Cai, Z., Sun, F., et al. 2023, *ApJ*, 942, L1  
 Yang, G., Papovich, C., Bagley, M., et al. 2024, ArXiv e-prints [arXiv:2307.14509]  
 Yu, S.-Y., Cheng, C., Pan, Y., Sun, F., & Li, Y. A. 2023, *A&A*, 676, A74  
 Zavala, J. A., Aretxaga, I., Dunlop, J. S., et al. 2018, *MNRAS*, 475, 5585

## Appendix A: SMG properties

**Table A.1.** Cumulative index for filter coverage in HST and JWST observations

Index	1	2	4	8	16	32	64	128	256	512	1024
HST	F275W	F336W	F435W	F475W	F606W	F814W	F850LP	F105W	F125W	F140W	F160W
JWST	F090W	F115W	F150W	F200W	F277W	F356W	F410M	F444W	F770W	F1800W	

Table A.2: Table summarising the AS2UDS and AS2COSMOS SMGs identified in the PRIMER survey. The table is only available in electronic form at the CDS.

## Appendix B: SEDs

A full version of Appendix B is available in electronic format on the Zenodo platform<sup>9</sup>.

<sup>9</sup> <https://zenodo.org/records/13805467>